LJMU Research Online

Sun, K, Xu, Z, Li, S, Jin, J, Wang, P, Yue, M and Li, C

Dynamic response analysis of floating wind turbine platform in local fatigue of mooring

http://researchonline.ljmu.ac.uk/id/eprint/20240/

Article

Citation (please note it is advisable to refer to the publisher's version if you intend to cite from this work)

Sun, K, Xu, Z, Li, S, Jin, J, Wang, P, Yue, M and Li, C (2023) Dynamic response analysis of floating wind turbine platform in local fatigue of mooring. Renewable Energy, 204. pp. 733-749. ISSN 0960-1481

LJMU has developed **LJMU Research Online** for users to access the research output of the University more effectively. Copyright © and Moral Rights for the papers on this site are retained by the individual authors and/or other copyright owners. Users may download and/or print one copy of any article(s) in LJMU Research Online to facilitate their private study or for non-commercial research. You may not engage in further distribution of the material or use it for any profit-making activities or any commercial gain.

The version presented here may differ from the published version or from the version of the record. Please see the repository URL above for details on accessing the published version and note that access may require a subscription.

For more information please contact researchonline@ljmu.ac.uk

http://researchonline.ljmu.ac.uk/

Dynamic Response Analysis of Floating Wind Turbine Platform in Local Fatigue of Mooring

Kang Sun[a] Zifei Xu[a,b] Shujun Li[a] Jiangtao Jin[a] Peilin Wang[a] Minnan Yue[a] Chun Li[a,c]

(a. University of Shanghai for Science and Technology, Energy and Power Engineering Institute, Shanghai 200093;
b. Liverpool John Moores University, Department of Marine and Mechanical Engineering, Liverpool, L3 3AF;
c. Shanghai Key Laboratory of Multiphase Flow and Heat Transfer in Power Engineering, Shanghai 200093)

Abstract: The moorings of the Floating Wind Turbine (FWT) platforms, long term suffering from the coupling loads of wind, waves and currents, are especially prone to structural fatigue. The purpose of this study is to mine effective information from the dynamic response of the FWT platform to achieve early damage detection for mooring health conditions. However, high nonlinearity of the FWT platform dynamic response, that is caused by the complexity of the working environment, hinders the accuracy of fatigue analysis and damage detection, Therefore, in this study, motivated by the accuracy of the chaotic features in quantifying nonlinearities and reliability of the convolutional neural network for feature extraction, an intelligent damage detection model, named Convolutional Neural Network-t-distribution Stochastic Neighbor Embedding (CNN-t-SNE), is proposed to automatically detect the damage magnitude of the moorings. Through analyzing the dynamics of FWT platform mooring from structure creep to failure, it is found that the yaw response is the most sensitive to structural damage. To examine the reliability of the proposed CNN-t-SNE method, the Lyapunov exponent and chaotic attractor quantify the nonlinearity of the features in the neural networks to indicate that the nonlinearity of the features decreases as the neural network layer deepens. Weaker nonlinear features help the damage detection model to locate and quantify the damage magnitude for the moorings of the FWT platform.

Key words: floating wind turbine; fatigue; convolutional neural network; dynamic response; pattern recognition

Nomenclature	
FWT	Floating Wind Turbine
t-SNE	t-distribution Stochastic Neighbor Embedding
CNN	Convolutional Neural Network
CNN-t-SNE	Convolutional Neural Network- t-distribution Stochastic Neighbor Embedding

1 Introduction

Energy reserves are plummeting sharply with the rapid development of human industrial civilization. In the meantime, environmental pollution and other issues are becoming more and more serious, so it is necessary to find an urgent solution to maintain sustainable development. Therefore, promoting energy transformation and looking for renewable energy have attracted widespread attention from all over the world [1]. As a renewable energy widely used by human beings, wind energy is one of the most promising renewable energy sources because of its abundant reserves, wide distribution, green and clean, easy development and utilization, etc [2].

Wind turbines are the best mechanical equipment for energy transformation. Heretofore, the onshore wind turbines have developed rapidly, and many scholars have put forward some control strategies to ensure the safety and stability of the wind turbine operation. In the literature [3], a new pitch controller is proposed by employing partial offline quasi-min-max fuzzy model-predictive control to investigate the variable-speed wind turbine performance, which can effectively adjust the generator speed so as to produce the rated power in the high wind speed range. Regarding the large-scale, geographically dispersed wind farm, literature [4] proposes an efficient distributed economic model predictive control strategy, which integrates the power tracking and economic optimization of the wind farm into one optimal control framework. It can effectively control the stability and security of renewable power system of the large-scale wind farm. However, with the deepening of the research on wind energy, onshore wind turbines will not generate energy all year round, because of poor wind speed and obstruction of some natural obstacles such as buildings and hills, resulting in countries around the world have begun to work on offshore wind turbines. At the same time, offshore wind energy also has the advantages of being close to the center of economic development, low transmission losses, etc, and is developing extremely rapidly. However, with the development of offshore wind turbines from epeiric sea to abyssal sea, the piled offshore wind turbine has been difficult to apply to the abyssal sea, so there is an urgent need to develop some more suitable offshore support structures [5]. Among them, floating wind turbines are gradually accepted by the wind energy field because of their applicability to deep sea areas and flexibility in construction and installation, and have been applied in a large number of projects, which are the main development direction at present and in future [6].

Heretofore, there has been lots of mature research to maintain safety and stability for onshore wind turbines, including developing condition monitoring systems for bearings, gearboxes, blades, and foundations. Dupuis [7] based on basic gearbox component geometry to develop an effective data-driven propagation model for health monitoring of onshore wind turbines. Dybala [8] adopted a diagnosis method based on empirical mode decomposition to identity bearing early-stage faults. However, for the most promising floating wind turbines, because of their high center of gravity and no fixed foundation, will be subject to wind, waves, currents, aerodynamic load and wind tilting moment during the working process, and the coupling effect among the components of the floating wind turbine system is relatively obvious [9]. In order to ensure that the floating wind turbine will not be displaced and capsized, it is connected to the anchor point on the sea floor through mooring, which can provide it with positioning and restoring force. However, because of the floating nature of the platform, the mooring is subjected to large time-varying tension. In addition, there is the long-term corrosion and wear of seawater, it affects the operational safety of the whole floating wind turbine system and even leads to catastrophic accidents such as platform damage, casualties and environmental pollution [10]. For example, in 2005, Hurricane Rita caused a tendon failure and eventual capsize of the tension leg platform Typhoon TLP in the Gulf of Mexico [11]. When the mooring fails, the dynamic response of a floating wind turbine increases, which can affect its operational safety. The above evidence shows that, especially for the foundation, the working environment between onshore wind turbine and offshore wind turbine leads to significant differences in the dynamic behaviors of the foundation, which means it is difficult to directly apply maintenance experience for onshore wind turbines to floating wind turbines.

Considering that the floating wind turbine is in extreme environments for a long time, the moorings are susceptible to creep due to high load and loading, causing its corrosion resistance and load carrying capacity to be reduced, and if not repaired in time, the moorings will easily fail and affect the operational safety of the floating wind turbine. Therefore, it is essential to analyze the dynamic response data of floating wind turbines to detect problems before mooring failure and to ensure that each mooring is always in a safe condition during the operation of floating wind turbines.

In recent years, floating wind turbine systems are subject to various failure risks and the research of platform dynamic response has gradually emerged. Li [12] studied the dynamic response of OC3-HywindSpar type floating wind turbines after a single anchor chain failure in rated sea state and found that wind turbines with anchor chain failure increase the risk of collision with neighboring wind turbines. Bae [13] analyzed the dynamic response of OC4-DeepCwind semi-submersible floating wind turbine after a single anchor chain failure, and the study showed that anchor chain failure causes long-distance drifting motion of the platform and has an effect on the anchor chain tension and nacelle yaw error. Yang [14] used the slender rod theory to simplify the riser and mooring cable, and established a coupling analysis method for deep-water floating structure-mooring system to study the coupling effect between the components. However, these studies only analyzed the dynamic behavior of floating wind turbines and did not contribute to the fatigue mechanism of mooring or how to diagnose fatigue damage.

Up to now, deep learning has been widely used in wind turbine blade fault diagnosis. Thereinto, Convolutional Neural Network has gradually received the attention of most scholars because of its powerful feature extraction ability and reliable and efficient classification ability. Kreutz [15] achieved accurate identification of blade icing conditions by CNN recognition of images on wind turbine blades; Cao [16] used CNN to learn and extract blade fault features, which can accurately detect problems such as blade aerodynamic and mass imbalance. Guo [17] fuses CNN and 3D vibration signals for blade crack diagnosis, and achieves high accuracy identification effect by establishing a crack sample database. There has been more research on the application of convolutional neural network in wind turbine operation diagnosis, but most of them focus on wind turbine blade and bearing gearbox, but few studies on floating wind turbine at sea, and the studies involving floating wind turbine mooring are especially rare. At present, wind power development "from land to sea, shallow sea to abysmal sea " has become a consensus for the academic and business community, the study of the stability and safety of floating wind turbines applicable to a broader sea is essential [18].

However, for floating wind turbines, the structural damage of blades or gearboxes can be migrated by referring to the prior maintenance knowledge and methods of land wind turbines, but due to the floating nature, the dynamic response changes caused by mooring creep lead to existing prior knowledge that cannot be used for data analysis and modeling of this unknown distribution.

Therefore, in order to solve the issues of the above study, the mooring system of ITI Energy Barge platform equipped with NREL 5 MW wind turbine is used as the research object in this paper.

In order to solve the issues in the current study, to develop a dynamic model for the ITI Energy Barge platform NREL 5 MW wind turbine model to study the dynamic behavior during the fatigue state of mooring system. Considering the nonlinear characteristics of FWT platforms dynamic responses, a new (CNN-t-SNE) damage identification model is established to detect mooring structure damage. The main contributions of the paper are as follows:

1. Analyze the potential relationship between the dynamic response of the floating wind turbine with different degrees of freedom and the damage of the mooring structure.
2. Development of an intelligent damage detection model, using CNN to mine potential information from chaotic attractor trajectories and quantify the relationship between structural damage and nonlinear strength by means of Lyapunov index.
3. The effect of the optimization function on the model convergence is investigated and the robustness of the proposed model in noisy environments is checked.

The remaining parts of this paper are organized as follows. A brief description of the floating dynamic model is given in Section 2. The intelligent damage detection method based on CNN-t-SNE is introduced in Section 3. In addition, Section 4 analyzes the superiority and generalization ability of the proposed model based on experimental data. The visualizations of the model are presented to show the features that have been learned by the developed model are also presented in this section. Finally, the conclusions are presented in Section 5, and in section 6, future work is introduced

Considering that the floating wind turbine platforms yawing response is more sensitive than other degrees of freedom when the mooring state changes, the platform yawing response data under each mooring damage is analyzed as diagnostic data. CNN is used to analyze the dynamic response data under different mooring creeps to determine whether creep occurs in the mooring and the location of the creeping mooring. The calculation results show that the response of each degree of freedom of the platform increases sharply from creep to failure, and the roll response, yaw response, surge response and sway response are most affected, the dynamic response of heave and pitch changes little. In addition, the mooring failure on the windward side has a greater impact on platform stability, while the leeward side has a smaller impact. Meanwhile, the deep learning model can deeply mine the information of creeping mooring and extract the pure signal. Based on chaos theory, by analyzing the attractor trajectories of the signals extracted by convolutional neural networks, we can find the real laws behind random phenomena, that is, we can quantitatively judge the nonlinear strength of dynamic signals. It is found that CNN diagnostic model can effectively extract creep information and realize intelligent diagnosis of whether the mooring is creeping and the position of creeping mooring, which provides technical support and realization way for floating wind turbine mooring health diagnosis. Meanwhile, considering the influence of environmental noise during the actual operation of floating wind turbines, the accuracy of fault identification is analyzed under different signal-to-noise ratios, and the computational results show that all maintain a high identification accuracy of more than 85%, and the iterative convergence is rapid.

2 Research Subjects

2.1 Model of floating wind turbine

Based on a 5 MW floating wind turbine developed by the National Renewable Energy Laboratory, the ITI Energy Barge platform was used as a research target. The complete system is shown in Figure 1 [19].

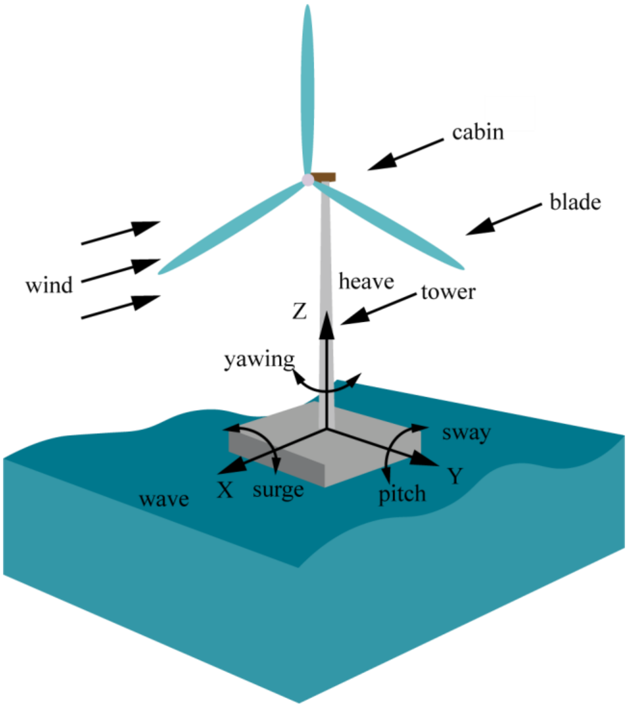

Figure.1 Floating wind turbine of Barge platform

The main parameters of the floating wind turbine and the ITI Energy Barge platform are shown in Table 1 and Table 2.

Table 1

Parameters of wind turbine

Parameters/Units	Value	Parameters/Units	Value
Power/MW	5	Cut-out wind speed/$m\cdot s^{-1}$	25
Number of blades/n	3	Hub diameter/m	3
Wind turbine diameter/m	126	Tower height/m	90
Rated speed/rpm	12.1	Wind wheel mass/kg	1.1×10^{5}
Cut-in wind speed/$m\cdot s^{-1}$	3	Tower mass/kg	3.5×10^{5}
Rated wind speed/ $m\cdot s^{-1}$	11.4	Nacelle mass/kg	2.4×10^{5}

Table 2

Parameters of ITI Energy Barge

Parameters/Units	Value	Parameters/Units	Value
Length × width/m	40×40	Number of cable guide holes/n	4
Draught depth/m	4	Number of moorings/n	8
Barycenter/m	-0.282	Transverse inertia/kg·m^2	7.269×10^8
Displacement/m^3	6×10^3	Longitudinal rocking inertia/kg·m^2	7.269×10^8
Mass/kg	5.452×10^6	Bow rocking inertia/kg·m^2	1.454×10^9

2.2 Mooring systems

The ITI Energy Barge platform is connected to the seabed anchor point through eight moorings in the guide holes on the four corners, and the top view of the platform is shown in Figure 2.

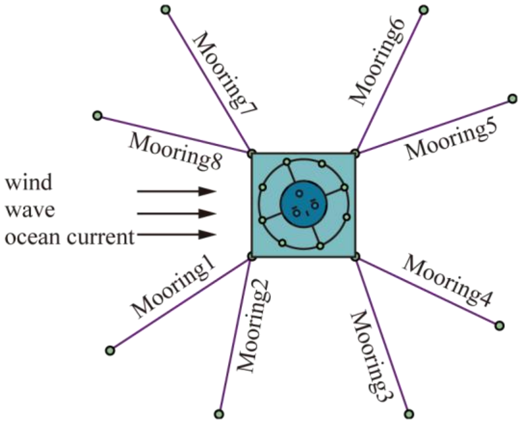

Figure.2 Schematic diagram of mooring

The mooring parameters are shown in Table 3 [20].

Table 3

Parameters of mooring

Fixed chain suspension line parameters/units	Value
Mass/kg·m^{-1}	129.5
Equivalent cross-sectional area/m^2	0.00636
Maximum tension/N	7.5×10^6
Axial stiffness/N·m^{-1}	7.5×10^8
Mooring length/m	473.3

2.3 Load and environmental parameters

In-service floating wind turbines in the extreme marine environment will be subject to wind, waves and currents and other loads, its blade by the wind load and floating platform by the waves and currents load is the most prominent [21].

2.3.1 Wind loading

The upper blade of the floating wind turbine is mainly subjected to wind load. In this paper, based on the blade element momentum theory, the induced velocity of the blade plane is solved using the dynamic inflow theory, and the magnitude of the angle of attack at each position along the blade expansion is calculated [22]. The induced velocity is:

$$v(r,\tilde{\psi}) = v_0 + v_s u\sin\tilde{\psi} + v_c u\cos\tilde{\psi} \tag{1}$$

Where v represents the induced velocity; r represents the radial radius of the blade; v_0, v_s and v_c are, respectively, the average, horizontal and vertical components of the induced velocity; u represents the ratio of radius; $\tilde{\psi}$ represents the yaw angle.

The thrust and torque on the blades are shown below:

$$\begin{cases} \mathrm{d}Q = \dfrac{1}{2}\rho c \dfrac{\left(\Omega r(1+b)\right)^2}{cos^2\theta}\left(C_l\, sin\theta - C_d\, cos\theta\right)\mathrm{d}r & \text{(2a)} \\ \mathrm{d}N = \dfrac{1}{2}\rho c \dfrac{U_\infty{}^2(1-a)^2}{sin^2\theta}\left(C_l\, cos\theta + C_d\, sin\theta\right)\mathrm{d}r & \text{(2b)} \\ C_l = 2F_L / (\rho_\infty V_\infty{}^2 \cdot c) & \text{(2c)} \\ C_d = 2F_D / (\rho_\infty V_\infty{}^2 \cdot c) & \text{(2d)} \\ C_x = C_l\, cos\theta + C_d\, sin\theta & \text{(2e)} \\ C_y = C_l\, cos\theta - C_d\, sin\theta & \text{(2f)} \\ a/(1-a) = 0.25\varpi_r\, sin^{-2}\phi(C_x - 0.25\varpi_r C_y{}^2\, sin^{-2}\phi) & \text{(2g)} \\ b/(1-b) = 0.25\varpi_r C_y\, sin^{-1}\phi\, cos^{-1}\phi & \text{(2h)} \end{cases}$$

Where Q represents the torque acting on the wind wheel; N represents the axial thrust force on the wind wheel; ρ represents the air density; Ω represents the blade speed; b represents the tangential induction factor; c represents the chord length of the wind turbine blade at the center of the hub; r represents the radial radius of the blade; θ represents the incoming angle of attack; C_l and C_d are, respectively, the lift coefficient and coefficient of resistance; a represents the axial induction factor; U_∞ represents the incoming flow rate; C_x represents the axial aerodynamic coefficient; F_L and F_D are, respectively, the forces perpendicular and parallel to the direction of the airfoil chord ; ϕ represents the velocity potential function; V_∞ represents the infinite distant velocity of wind flow; ρ_∞ represents the infinite distant air density; C_y represents the tangential aerodynamic coefficient; ϖ_r represents the leaf chord length solidity.

From equation (2), the lift coefficient and coefficient of resistance can be taken out from equations (2c) and (2d), axial induction factor and tangential induction factor can be taken out from equations (2e-2h).

2.3.2 Wave loading

There are three methods of wave load calculation, including strip theory, Morison equation and radiation/diffraction theory. The strip theory is suitable for solving the wave load of the ship, and the Morison equation are mostly used when the floating body has no obvious influence on the incident wave field. Because the Barge platform is a large scale structure, its effect on the cannot be ignored, and the needs to be considered, so this paper solves the wave load of the platform in the water based on the radiation theory and the diffraction theory to assume the fluid is incompressible, inviscid and spinless, as shown in Figure 3. S_B is wet surface, S_F is wave free surface, the seafloor S_D and the liquid surface S_C at infinity form a semi-infinite space.

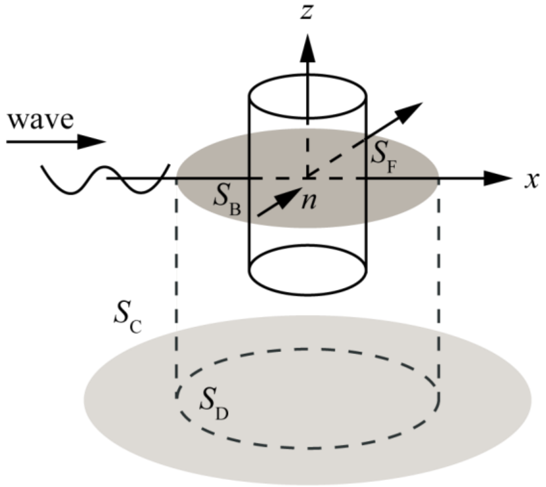

Figure.3 Action of waves on the floating objects

The velocity potential function is shown as follows [23]:

$$\phi = \phi_\mathrm{i} + \phi_\mathrm{d} + \sum_{\mathrm{j}=1}^{6} \phi_\mathrm{r} \tag{3}$$

Where ϕ_i, ϕ_d and ϕ_r are, respectively, the incident potential, diffraction potential and radiation potential.

The above functions need to satisfy the Laplace equation and the boundary condition:

$$\begin{cases} \partial^2\phi / \partial x^2 + \partial^2\phi / \partial y^2 + \partial^2\phi / \partial z^2 = 0 & \text{(4a)} \\ \partial\phi / \partial z\big|_{z=d} = 0 & \text{(4b)} \\ g\partial\phi / \partial z + \partial^2\phi / \partial t^2 = 0 & \text{(4c)} \\ \partial\phi / \partial z = \partial\eta / \partial t + (\partial\eta / \partial x)\cdot(\partial\phi / \partial x) + (\partial\eta / \partial y)\cdot(\partial\phi / \partial y) & \text{(4d)} \\ \partial\phi / \partial \boldsymbol{n} = 0 & \text{(4e)} \end{cases}$$

where g is the acceleration of gravity; η is the incident wave surface function; d represents the sea depth; $\boldsymbol{n}$ is the external normal vector of wet surface of floating body.

Therefore, the wave force and wave moment of the Barge platform can be recorded as:

$$F_\mathrm{W} = \iint_{S_\mathrm{B}} -p\boldsymbol{n}\mathrm{d}s \tag{5}$$

$$M_\mathrm{W} = \iint_{S_\mathrm{B}} -p(\boldsymbol{r} \times \boldsymbol{n})\mathrm{d}s \tag{6}$$

where F_W represents the wave force; M_W represents the sea waves moment; s represents the platform wetted surface equation; p represents the water pressure on wetted surface, $p = -\rho_\mathrm{water}\partial\phi / \partial t$; ρ_water represents the sea water density; $\boldsymbol{r}$ represents the structure surface to base point vector.

2.3.3 Current loading

Because of the slow speed of the current, its force on the offshore structure is mainly reflected as drag force, which can be written as [24]:

$$F_c = \frac{1}{2}\rho_s C_D A U_o^{\ 2} \qquad (7)$$

where ρ_s is the sea water density; C_D is the drag coefficient; A is the equivalent area of platform along the direction of coastal flow; U_o is the flow velocity.

2.3.4 Environmental parameters

According to the design requirements of IEC 61400-3 offshore wind turbine, this paper adopts the method proposed by Jonkman [25]. Considering that the wind and waves are incident in the same direction at the same time, the angle of incidence is -180°, assume that the ocean current is uniform, with a velocity of 0.8 m/s., the wind speed is 11.4 m/s, and the wind spectrum is Kaimal wind spectrum. The results are shown in figure 4.

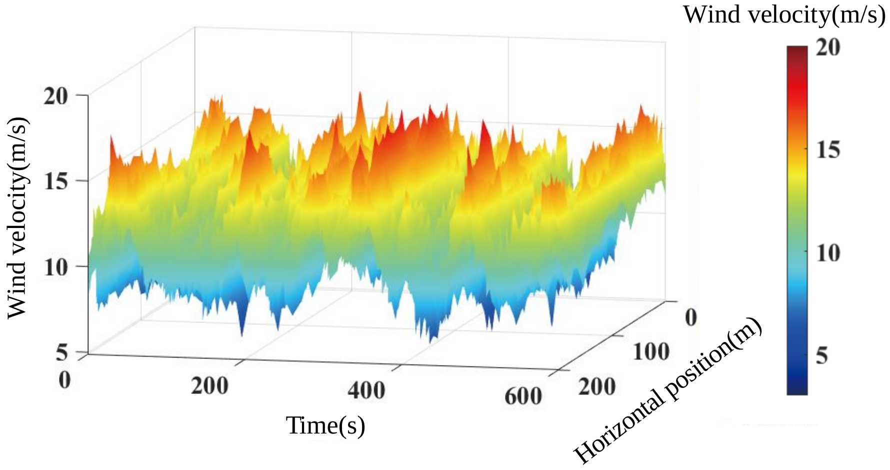

Figure.4 Turbulent wind spectrum

The waves are irregular waves generated based on the P-M spectrum. The spectral peak period is 10.1 s, the significant wave height is 6 m, and the time travel curve of the irregular wave is shown in Figure 5

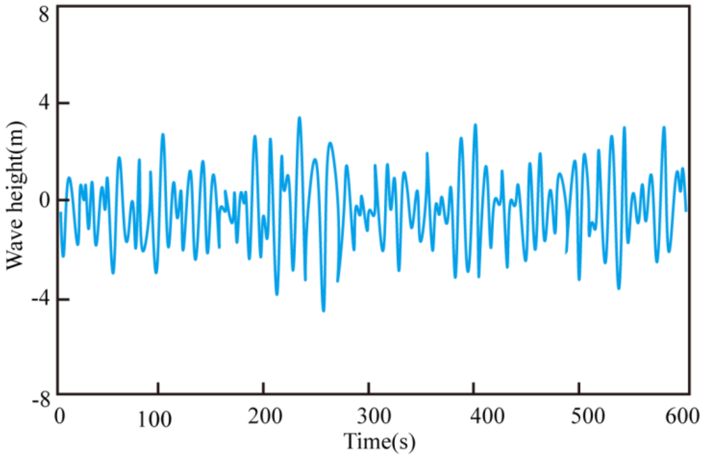

Figure.5 Time series of wave height

3 Theoretical Basis

3.1 Convolutional Neural Networks

Convolutional neural network, as a typical feed-forward neural network, is an end-to-end data processing method. With powerful feature extraction capability, its essence is to construct multiple filters to extract feature information hidden in the original data layer by layer, with local acceptance domain, shared parameter weights and sparse connections, which can effectively avoid data redundancy and overfitting problems. The traditional CNN model mainly includes convolutional layer, activation function, pooling layer and fully connected layer [26].

3.1.1 Convolutional layer

Convolution, as the core of CNN, extracts the original data through the rectangular convolution kernel, combines the parameter sharing mechanism, performs convolution operation on the original data with the convolution kernel, and calculates and outputs the characteristic data [22]. The expression is:

$$x_{i+1} = \boldsymbol{W} \otimes x_i + \boldsymbol{b}_i \tag{8}$$

where x_{i+1} and x_i are, respectively, the data after the convolution layer and data before the convolution layer; $\otimes$ represents the convolution Operators; $\boldsymbol{W}$ represents the weight matrix; $\boldsymbol{b}_i$ represents the offset.

3.1.2 Activation functions

In order to make a nonlinear transformation of the convolved data, activation functions are used for processing. The commonly used ones are Tanh, Sigmoid and Relu activation functions, and in this paper, the Relu function is chosen, which can avoid the gradient disappearance problem of Sigmoid function and improve the computational efficiency [22]. Equation (8) is transformed as:

$$y_i = f(x_{i+1}) = f(\boldsymbol{W}_i \otimes x_i + \boldsymbol{b}_i) \tag{9}$$

where y_i represents the data after transformation; $f(\cdot)$ represents the Relu activation function.

3.1.3 Pooling layer

In order to solve the dimension disaster caused by the increase of data volume and dimension after the data is extracted by convolution layer. On the basis of ensuring that the original feature information is not lost, the pool function is used to process the data extracted from the convolution layer, which can not only avoid the overfitting problem, but also choose the main representative features. In this paper, the maximum value pooling is used to select the maximum value from the region corresponding to the pooling kernel as the representative value, which can reflect the most significant features of the original data. The expression is shown as follows:

$$\text{max - pooling}\left(f[i-1], f[i], f[i+1]\right) = max\left(f[i-1], f[i], f[i+1]\right) \tag{10}$$

where max - pooling is the maximum pooling; $f[i]$ is the i-th pixel value; $\max(\cdot)$ is the maximum value.

3.1.4 Fully connected layer

The fully connected layer is the connecting transition part between the convolutional pooling layer and the sorter, and integrates distinguishing feature information by connecting with all neurons in the convolutional pooling layer. The feature information input to the fully connected layer after the convolutional pooling layer process can be transformed into a one-dimensional feature vector, and finally a Softmax classifier is used for classification. The expression is shown below [23]:

$$o(x) = f\left(\boldsymbol{W}x + \boldsymbol{b}\right) \tag{11}$$

Where $o(x)$ represents the full connection layer output; x represents the full connection layer input; $\boldsymbol{W}$ represents weight matrix of fully connected layer; $f(\square)$ represents the Softmax activation function.; $\boldsymbol{b}$ represents the tangential induction factor.

3.1.5 Learning Tips

In order to prevent the overfitting problem of CNN networks and improve the diagnostic classification accuracy, some learning techniques are usually used to improve CNN performance. After long-term practice, it is concluded that Batch Normalization(BN) , data augmentation and Dropout techniques are widely used to process the network structure. In this paper, BN and Dropout techniques are used to process the original data. Among them, BN technique is to process the original data into normative data of the same order of magnitude to prevent gradient disappearance and gradient explosion problems. Dropout technique is to randomly discard a certain percentage of neurons in the network model to let a very small portion of abnormal data into the model learning and reduce its impact on the model [27].

The hyperparameters of the CNN model have significant effects on the fault diagnosis accuracy, among which the activation function, learning rate, optimizer, the number of convolutional layers and pooling layers are the most significant. To investigate the effects of different parameters on the model performance, a 3-layer CNN model with relatively high classification accuracy was preestablished as the base model after several debuggings. The model hyperparameters were modified to determine the optimal CNN model. The initial model uses the Rmsprop optimizer with a learning rate of 0.1 and 50 of iterations.

3.1.6 Activation function

The fault classification accuracy and training time vary greatly when different activation functions are used for each convolutional layer. Traditional methods are often set according to human experience, which is more random. In order to select the best combination of functions, the effects of three commonly used activation functions (Tanh, Elu, and Relu) are compared according to the initial model, and the results are shown in Table 4.

Table 4

Comparison of activation function

Experiment	C1	C2	C3	Accuracy rate /%	Time/s
1	Elu	Elu	Elu	94.25	109
2	Relu	Elu	Elu	78.25	101
3	Tanh	Elu	Elu	96.75	102
4	Relu	Relu	Relu	98.91	96
5	Relu	Tanh	Relu	96.75	103
6	Relu	Elu	Relu	98.25	104

7	Tanh	Tanh	Tanh	96.50	118
8	Tanh	Tanh	Elu	97.00	121
9	Tanh	Tanh	Relu	98.52	90

As can be seen from Table 4, in terms of accuracy, Experiment 3 is the highest, reaching 98.91%, indicating that the best results are obtained when the Relu function is used for all the convolutional layers; in terms of efficiency, it can be seen from Experiments 1, 2, 3, Experiments 4, 5, 6 and Experiments 7, 8, 9 that the Relu function is the least time consuming for all the convolutional layers. Therefore, it can be seen that the CNN network has the best efficiency when the Relu function is used as the activation function.

3.1.7 Learning rate

The learning rate is another important factor that affects the performance of CNN models. If its value is too small, the model convergence speed decreases; if it is too large, the training model oscillates and the optimal solution of parameters oscillates back and forth, and if it is too large, the CNN network cannot be trained properly. The Relu function is used for the activation function, and the learning rates of 0.0001, 0.001, 0.01 and 0.1 are selected in order by exponential scale for the test, and the number of iteration are 50, 70 and 100 respectively. The results are shown in Figure 6.

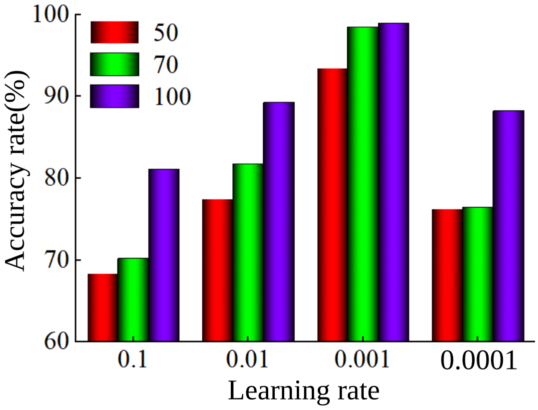

Figure.6 The effect of learning rate on accuracy

From Figure 6, it can be seen that the fault classification accuracy is proportional to the number of iterations, and when the learning rate is 0.001, the fault classification accuracy is the highest in all, close to 100%, so 0.001 is used as the CNN model learning rate with the highest efficiency.

3.1.8 Optimizer

The choice of optimizer plays an extremely important role in CNN training, which is related to the ability to converge quickly and achieve high recall ratio and precision degree. The most commonly used Adam, RMSprop and SGDM optimizers for current CNN models were compared and calculated, and the average value of ten experiments was taken, and the results are shown in Figure 7.

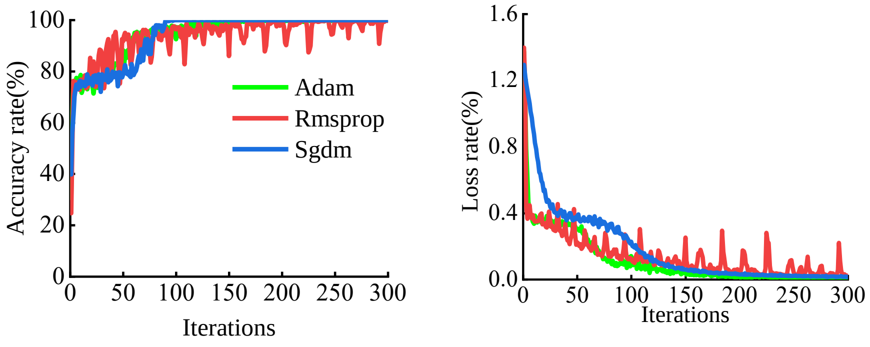

(a) Accuracy rate (b) Loss rate

Figure.7 The comparison diagram of optimizer performance

As can be seen above, in terms of training time and accuracy rate, when SGDM optimizer is used, the fault classification accuracy and loss rate have been stabilized at the number of iterations of 70, and the accuracy reaches 99% and the loss rate is close to 0. The performance is significantly better than other optimizers.

3.1.9 Topological structure

To investigate the effects of the number of convolutional layers, pooling layers and pooling type on the accuracy, three CNN topologies were designed using average pooling and max pooling, respectively, and the comparison experiments were conducted with and without Data Augmentation (DA), Batch Normalization (BN), and Dropout technology, and the results are shown in Table 5.

Table 5

Topological structure of CNN

Type	Groups	Pool type	Number of convolution layers and pooling layers	Accuracy rate /%	
				Training set	testing set
Common strength	A1	average pooling	3	73.35	74.75
	A2		4	92.00	94.5
	A3		5	72.89	75
	A4	max pooling	3	82.75	83.25
	A5		4	98.23	96.12
	A6		5	79.50	76.5
DA、BN、Dropout	B1	average pooling	3	73.25	74
	B2		4	91.23	92.79
	B3		5	73.75	75
	B4	max pooling	3	67.75	70
	B5		4	98.69	99.87
	B6		5	83.25	77.75

From Table 5, we can see that the classification accuracy of the 3-layer CNN network does not exceed 85% in both the training and testing sets because of the simple structure and the difficulty in extracting enough feature data; comparing A5 with B5, we can see that although the accuracy of the 4-layer CNN network with common strength reaches 98.23% in the training set, it is only 96.12% in the test set, which is an overfitting phenomenon. When the convolutional pooling reaches five layers, the accuracy of the training and testing sets is lower than that of the four-layer network, because the sample size is smaller and the network structure is prone to overfitting and gradient disappearance.

The training results are shown in Figure 8.

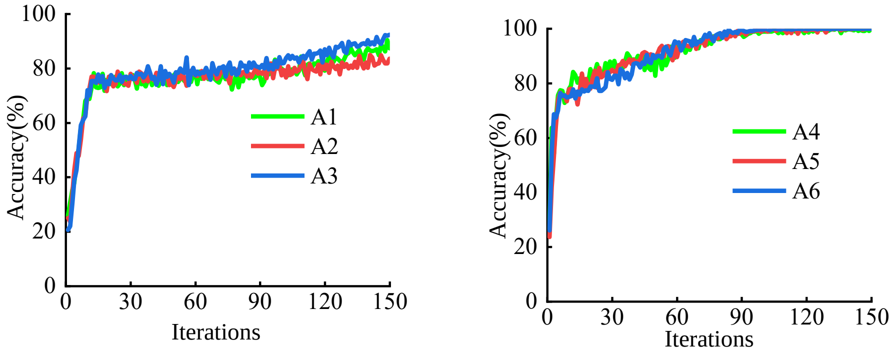

(a) Common strength /Average pooling

(b) Common strength /Max pooling

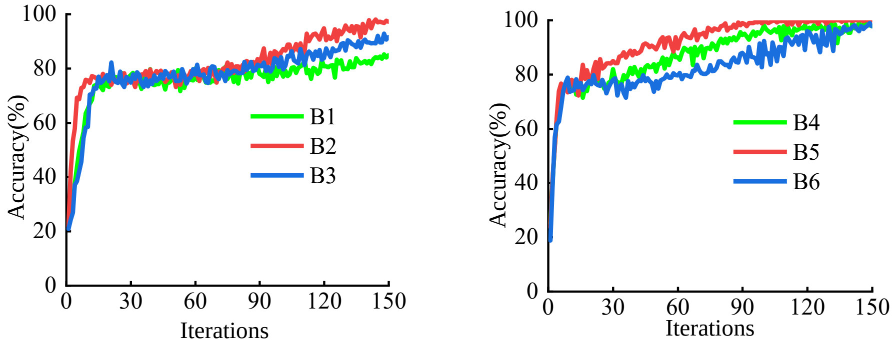

(c) DA、BN、Dropout/Average pooling

(d) DA、BN、Dropout/Max pooling

Figure.8 Comparison of accuracy of different CNN structures

From A5 in Fig. 8(b) and B5 in (d), it can be seen that using DA, BN, and Dropout techniques can improve the classification accuracy in a small range and effectively improve the overfitting problem.

3.1.10 CNN model architecture

For the mooring creep dynamic response data analyzed in this paper, the CNN model framework is designed as shown in Figure 9. The model parameters are shown in Table 6.

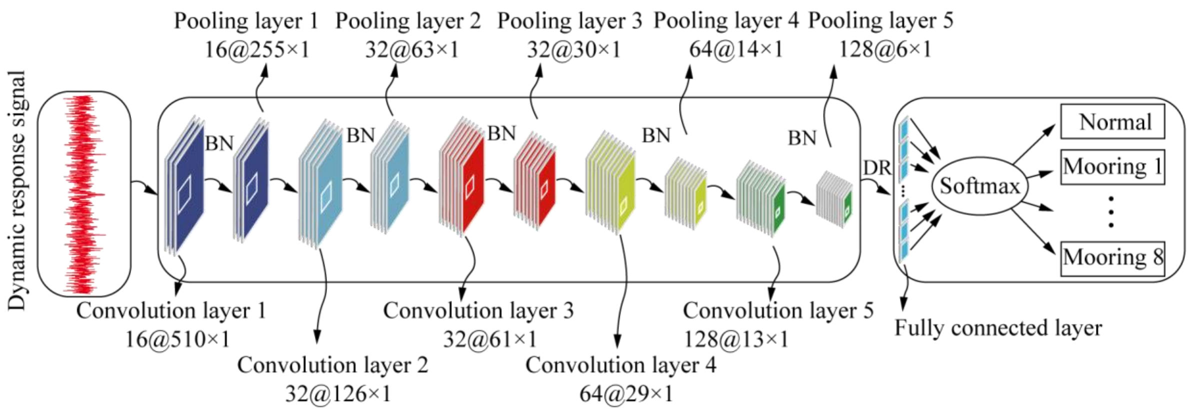

Figure.9 The model of CNN

Table 6

Parameters of model

Network Layer	Number and size of convolution kernels	Pooling area	Step length	Network layer output
Input Layer	-	-	-	1@2048×1
Convolutional layer C1	16@11×1	-	[4 1]	16@510×1
Pooling layer S1		[2 1]	[2 1]	16@255×1
Convolutional layer C2	32@5×1	-	[2 1]	32@126×1
Pooling layer S2	-	[2 1]	[2 1]	32@63×1
Convolutional layer C3	32@3×1	-	[1 1]	32@61×1
Pooling layer S3	-	[2 1]	[2 1]	32@30×1
Convolutional Layer C4	64@2×1	-	[1 1]	64@29×1
Pooling layer S4	-	[2 1]	64@14×1	
Convolutional Layer C5	128@2×1	-	[1 1]	128@13×1
Pooling Layer S5	-	[2 1]	[2 1]	128@6×1
Dropout layer	-	-	-	128@6×1
Fully connected layer	-	-	-	9@1×1

3.2 Chaos theory

As an important branch of modern nonlinear scientific research, fractals can reflect the self-similarity between the parts of a system and the whole, and can quantitatively describe the fractal characteristics of nonlinear systems. Chaos, as a fractal on the time scale, has the characteristics of sensitivity, dimensionality, randomness and universality, and can analyze the unstable discrete processes of nonlinear dynamical systems [26].

3.2.1 Phase space reconstruction

Phase space reconstruction is a method proposed by Packard to restore the nonlinear characteristics of a system by reconstructing attractor trajectories [28].To analyze the dynamics characteristics of dynamic response signal, a one-dimensional time series $\{y_i \mid i = 1, 2, \cdots N\}$ is embedded in a d-dimensional space to obtain the phase point $\boldsymbol{X}$:

$$\boldsymbol{X} = \begin{bmatrix} x_1 \\ x_2 \\ \vdots \\ x_N \end{bmatrix} = \begin{bmatrix} y_1 & y_{1+t} & y_{1+2t} & \cdots & y_{1+(d-1)t} \\ y_2 & y_{2+t} & y_{2+2t} & \cdots & y_{2+(d-1)t} \\ \vdots & \vdots & \vdots & \vdots & \vdots \\ y_N & y_{N+t} & y_{N+2t} & \cdots & y_{N+(d-1)t} \end{bmatrix} \tag{12}$$

where N represents the maximum number of one-dimensional time series; t represents the delay time; d represents the embedding dimension, $d \geq 2r+1$; r represents the number of system independent variables.

Delay time and embedding dimension have significant effects on the results. If d is too small, the attractor cannot be fully expanded and the phenomenon of mixing occurs; if it is too large, the computational efficiency decreases and noise is introduced, which makes it difficult to reflect the dynamics. If t is too small, each coordinate lacks independence; if it is too large, the complexity of each coordinate at different times increases.

Considering that the Cao method [29] is applicable to signals with small sample size and the mutual information function method [30] can reflect the correlation of data, the Cao method and the mutual information function method are used to calculate the embedding dimension and delay time, and they are used as a combination of parameters to construct the chaotic phase diagram.

3.2.2 Lyapunov Exponent

Chaos theory can reflect the nonlinear interactions among the components in a dynamic system to discover the real laws in the stochastic phenomena. Lyapunov exponent is used to describe the separation speed of two adjacent points of a chaotic system [24]. Liouville theorem states that for a conservative system the volume of the phase space does not change with time [31]. However, for a dissipative system, the volume of the phase space generally shrinks gradually with time due to the presence of dissipation items in the equations. The contraction of the volume of the phase space can be in all directions; or it can be an elongation in one direction and a contraction in the remaining directions, but the final volume is smaller than the initial volume. During the whole process, phase trajectories contract due to dissipative effects, but repel each other when they are close to each other, so that they eventually fold back and forth countless times within a finite range, forming a complex state of motion - chaos. Then the Lyapunov exponent is introduced to quantitatively characterize the speed of separation of two infinitely close points with time.

Assuming that the Jacobi matrix of the system exists everywhere, if the system is given a small disturbance $\Delta Z(a_0)$ at moment a_0, and the disturbance of the system becomes $\Delta Z(a)$ at moment a, the Lyapunov exponent is defined as:

$$\lambda = \lim_{a \to \infty} \frac{1}{(a - a_0)} \ln \left\| \frac{\Delta Z(a)}{\Delta Z(a_0)} \right\| \tag{13}$$

The Lyapunov exponent represents the tendency to separate or approach at an exponential rate between adjacent discrete points caused by each iteration on average over the course of many iterations, that is, the emissivity of average index number between adjacent trajectories. In a n-dimensional phase space, since the disturbance varies in all n directions, the system has n Lyapunov exponent.

The Lyapunov exponent can be used to determine whether the motion of the system is deterministic or chaotic. If the Lyapunov exponent of the system is positive, the motion of the system is chaotic; while the Lyapunov exponent is negative, the motion is periodic; and if the Lyapunov exponent is zero, the motion of the system is periodic motion or quasi-periodic motion.

The floating wind turbine has many parts, such as mechanical moving parts and electrical working parts. During the working process, there are very complex coupling relationships between the vibrations of different parts and components as the working state changes. In these relationships, there are also some changes with uncertainty, which will lead to the vibration signal of the floating wind turbine platform showing non-linear and non-smooth characteristics, in a chaotic state. However, although the structure of floating wind turbine is complex, the form of equipment failure is limited, so the motion trajectory of the system can only be contracted in a certain area, which is the boundedness of chaotic motion.

From the above analysis, we can see that the working system of a floating wind turbine is a nonlinear system, which may generate chaotic motion under certain conditions. Therefore, we can use the Lyapunov exponent, which reflects the characteristics of chaotic motion, to study the dynamic response signal of the floating wind turbine mooring when creep occurs, so that we can discriminate the mode and degree of its failure.

There are many methods for calculating the Lyapunov exponent, which are broadly grouped into two categories: the analytical method and the trajectory tracking method. Among them, the basic principle of the analytical method is a function is used to model the system and estimate the Jacobi matrix, which leads to the Lyapunov exponent.The trajectory tracking method follows the two orbits of the system directly from the definition of the Lyapunov exponent to obtain the Lyapunov exponent. The trajectory tracking method is valued because it is not as susceptible to the topological structure of the system as the analytical method. With the aid of the present advanced computer technology, solving the Lyapunov exponent by both types of methods is relatively straightforward.

In order to quantitatively represent the chaotic characteristics of the system, this paper reflects the characteristic information of the nonlinear response signal based on the Lyapunov exponent λ. In the actual calculation of the Lyapunov exponent, the most widely used is the famous Wolf algorithm, whose basic idea is to first reconstruct the univariate time series in phase space, and then estimate the Lyapunov exponent by evolution based on phase trajectory, phase area, phase volume, etc [32]. The main steps are as follows:

(1) Based on the delay time and embedding dimension determined in Section 3.2.1, the phase space reconstruction is performed to obtain the $N*d$ dimensional phase space.

(2) In the reconstructed N*d dimensional phase space, a point $\boldsymbol{X}_0$ is arbitrarily selected, and then the nearest point $\boldsymbol{X}_0^{'}$ is found in this phase space, and the distance between the two points is recorded as D_0. As time evolves, the distance between the two tracks starting from $\boldsymbol{X}_0$ and $\boldsymbol{X}_0^{'}$ will change, and the distance between the two points after one calculation cycle is $D_0^{'}$; and the angle between these two distance vectors is guaranteed to be as small as

possible. After that, the above process is repeated M times until the end of the time series. The Lyapunov exponent of the system is calculated as follows:

$$\lambda = 1/\left(T_M - T_0\right)\sum_{i=0}^{M}\ln(D_i^{'}/D_i) \tag{14}$$

where T_0 represents the start time of iteration; T_M represents the total iteration time; D_i represents the distance between the origin and the reconfiguration point; $D_i^{'}$ represents the distance between the origin and the reconstructed point at the next moment; M represents the total number of iterations.

3.2.3 Diagnostic Process

In this paper, deep learning and chaos theory are used to analyze the platform bow-rocking response data of each mooring creep phase, focusing on whether creep occurs in the mooring and the location of the creeping mooring. The specific diagnosis process is shown in Figure 10.

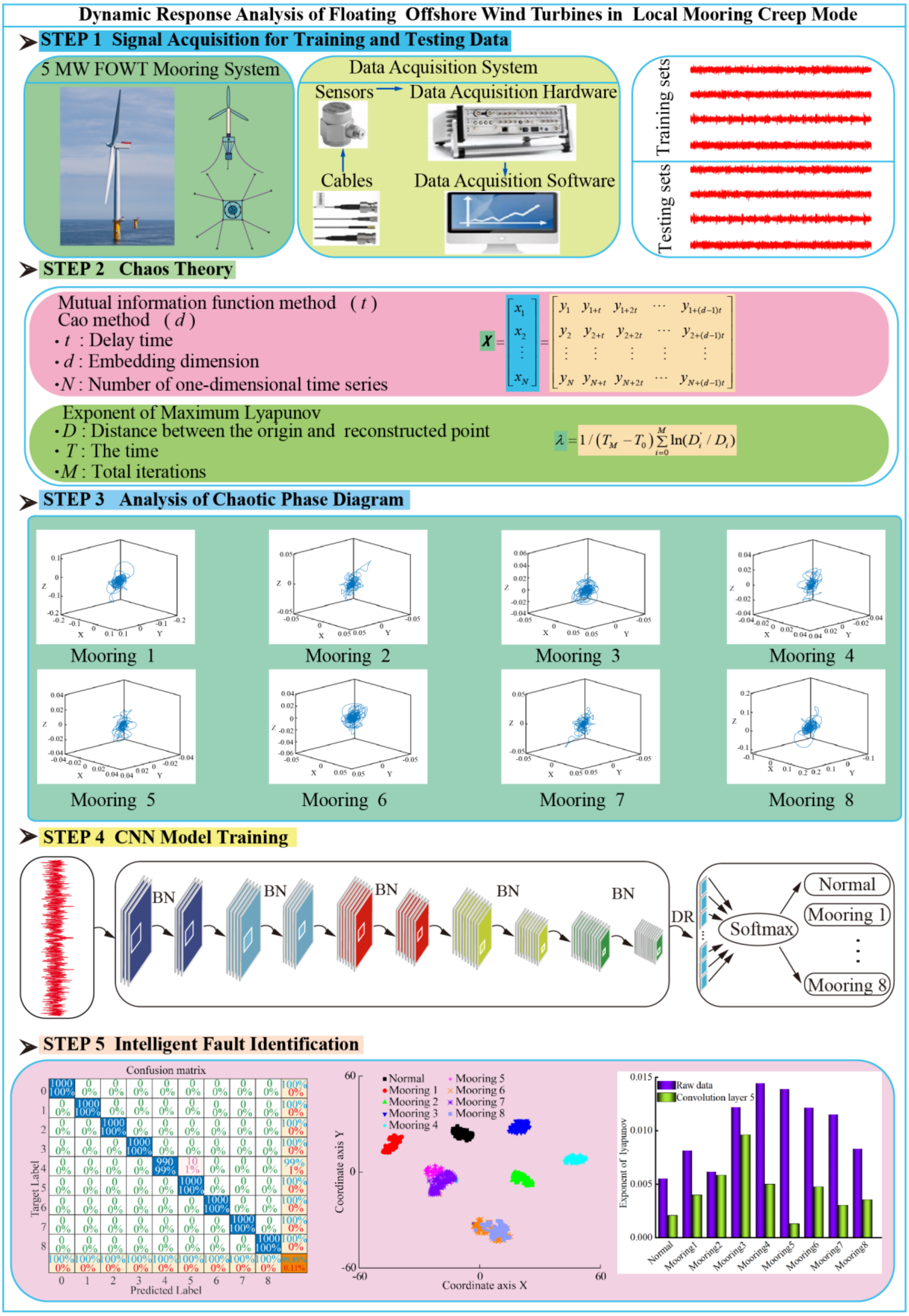

$$X=\begin{bmatrix}x_1\\x_2\\\vdots\\x_N\end{bmatrix}=\begin{bmatrix}y_1 & y_{1+t} & y_{1+2t} & \cdots & y_{1+(d-1)t}\\ y_2 & y_{2+t} & y_{2+2t} & \cdots & y_{2+(d-1)t}\\ \vdots & \vdots & \vdots & \vdots & \vdots\\ y_N & y_{N+t} & y_{N+2t} & \cdots & y_{N+(d-1)t}\end{bmatrix}$$

$$\lambda=1/(T_M-T_0)\sum_{i=0}^{M}\ln(D_i'/D_i)$$

Figure.10 Diagnosis flowchart of mooring

4 Results and Analysis

4.1 Dynamic response of FWT

In order to ensure the safe and stable operation of the floating wind turbine, mooring is needed to provide the restoring force for it. When the mooring fails by creep, its length and stiffness change slightly, and the restoring force provided by the mooring for the platform changes, which in turn affects the dynamic response of the platform. Considering that the dynamic response of the wind turbine platform is the strongest when the sea wind, waves and currents impact in the same direction, the mooring is subjected to the greatest load and the most violent tensile force fluctuations, and the possibility of failure is greater [33], so the sea wind, waves and currents are set to impact perpendicular to the wind turbine plane.

Due to the symmetrical distribution of eight moorings on the Barge platform, the dynamic response of the platform when creep and failure occurred in four of the moorings was investigated. The dynamic response of each mooring was analyzed in six degrees of freedom in normal, creep and failure conditions under wind and wave action, and the maximum response amplitude of the four moorings in three stages was studied. The results are shown in Figure 11.

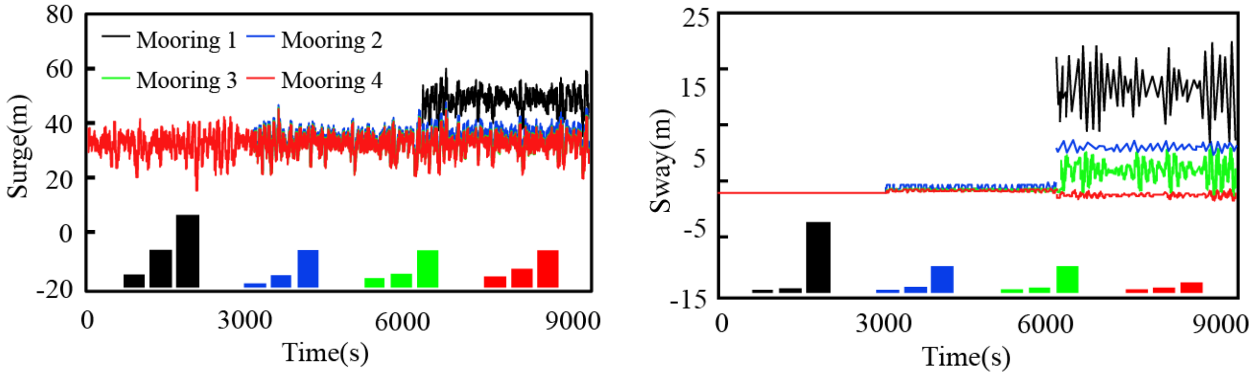

(a) Surge

(b) Sway

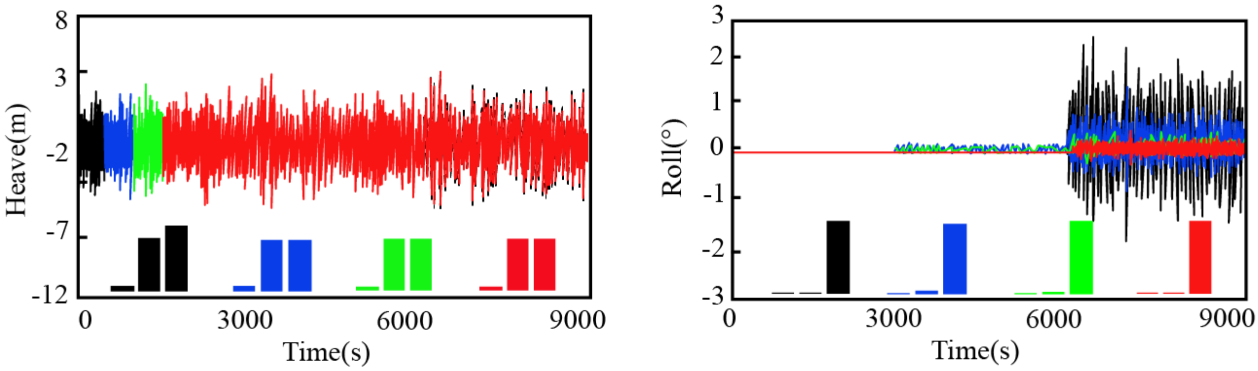

(c) Heave

(d) Rolling

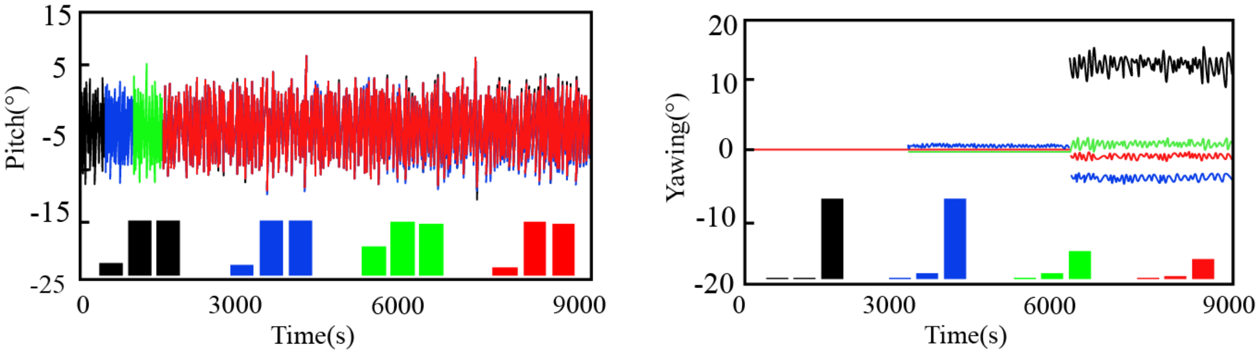

(e) Pitch

(f) Yawing

Figure.11 Floating wind turbine platform six degrees of freedom response

As can be seen from Figure 11, 0~3000s is the dynamic response of the floating wind turbine platform when the mooring is normal, 3000~6000s is the dynamic response of the platform after mooring creep, and 6000~9000s is the dynamic response of the platform after mooring failure. The bar graphs below the curves indicate the maximum response amplitude of the four moorings in the above three stages in corresponding colors, respectively.

The dynamic response of the platform in the three stages of normal, creep and failure is analyzed in Fig. 11a~Fig. 11e, and the dynamic response curves and maximum response amplitudes of the platform in the six degrees of freedom of surge, sway, heave, roll, pitch and yaw are compared.

It can be found that the dynamic response of the platform in all six degrees of freedom increases to different degrees after the creep and failure of the mooring. The results are as follows: ① For each degree of freedom, the roll, yaw, surge and sway are most affected by the change of mooring state, while the heave and pitch are less affected. The increase of surge and sway response is due to the uneven force on the platform laterally and longitudinally after the change of mooring state, while the increase of roll and yaw response is due to the uneven force on the platform after the change of mooring state, which causes the change of torque on the platform. ② The dynamic response of the platform increased slightly after mooring creep, but the increase was small; after mooring failure, the response of the platform increased sharply, most obviously in surge, sway, roll and yaw. ③ Comparing the dynamic response of the platform after the change of mooring state in different positions, it can be seen that the change of mooring state in different positions has different effects on the stability of the platform, among which the moorings closer to the windward side (moorings 1 and 2) have greater effects, and the moorings far from the windward side (moorings 3 and 4) have relatively smaller effects.

From the above analysis, it can be seen that during the mooring creep phase, the response of the platform in each degree of freedom changes very little, while the response in each degree of freedom increases sharply after mooring failure, when the upper part of the wind turbine operation will be greatly affected. The study in the literature [34] showed that the instantaneous thrust and power of wind turbines in the case of surge and pitch produce drastic changes, and the magnitude of such changes increases with the increase of the amplitude of surge and pitch. Among them, the surge motion with an angular displacement amplitude of 1° has a thrust variation of 12.65%, while the power variation is 30.98% higher. With the increase in the angular displacement amplitude of the surge motion, power shows a more sensitive change, which will lead to a significant increase in the blade shimmy and blade bending moment of floating wind turbines. In addition, due to the increased force on the wind turbine, the tower and the remaining mooring safety will be directly affected. Therefore, by diagnosing the dynamic response data of the floating wind turbine platform and discovering the mooring problems at the stage of mooring creep, it is crucial to prevent mooring failure in advance and ensure the structural safety and normal operation of the floating wind turbine.

When the mooring state is changed, the platform yaw response is more sensitive than the dynamic response of other degrees of freedom, so the platform yaw response data of each mooring creep phase are analyzed. The time domain and frequency domain plots of the platform yaw response under different mooring creep are shown in Figure 12.

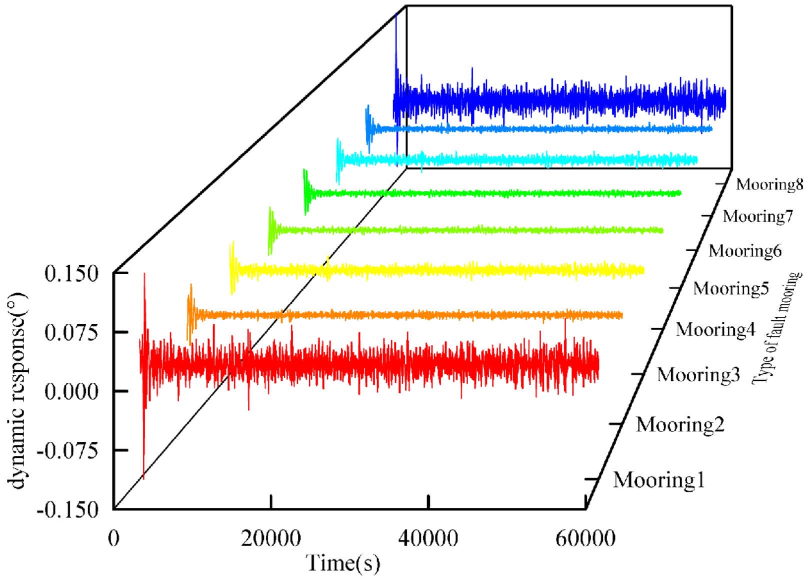

(a) The time domain

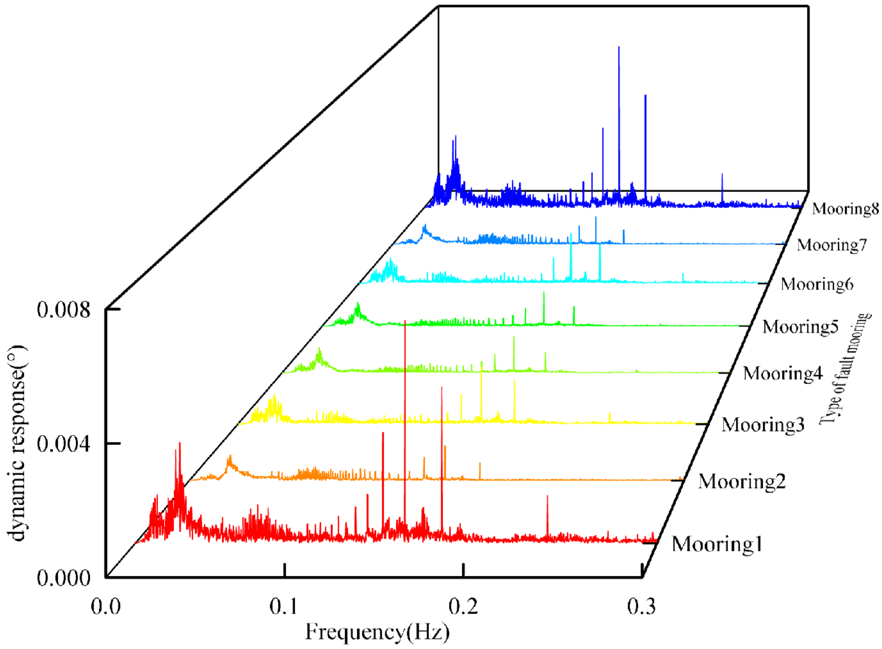

(b) The frequency domain

Figure.12 Platform yaw response under different mooring condition

As shown in Figure 12, during each mooring creep period, there is no significant difference between the time-domain and frequency-domain curves of the platform's dynamic response, so it is impossible to determine whether or not the creep occurs during mooring, and it is impossible to accurately determine the position of the creep moorings. In order to extract the effective fault characteristics, the three-dimensional attractor trajectories of the mooring creep data were plotted based on the phase space reconstruction method, and the chaotic characteristics of each mooring dynamic system were analyzed, and the optimal delay time and embedding dimension were calculated by using the Cao method [26] and the mutual information function method [27], and the results are shown in Table 7.

Table 7
The optimal parameters including delay time and embedded dimension

Mooring type	Normal	1	2	3	4	5	6	7	8
Delay time	8	20	2	21	21	21	21	22	20
Embedding dimension	8	4	4	4	3	3	4	4	4

The attractor trajectories of each mooring are shown in Figure 13.

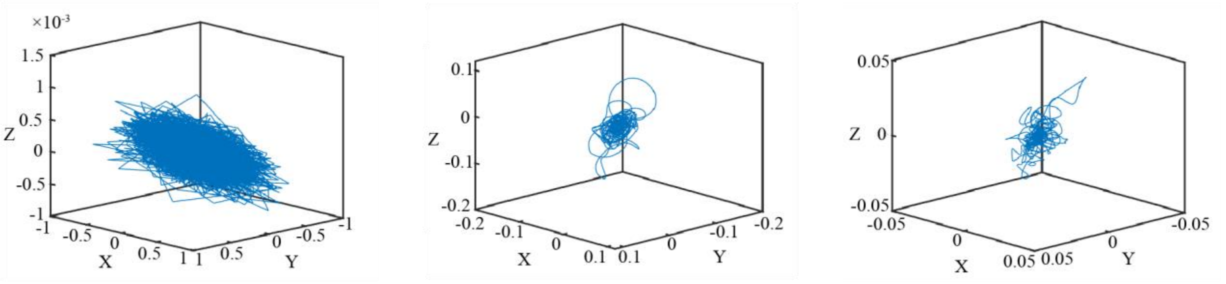

(a) Normal (b) Mooring 1 (c) Mooring 2

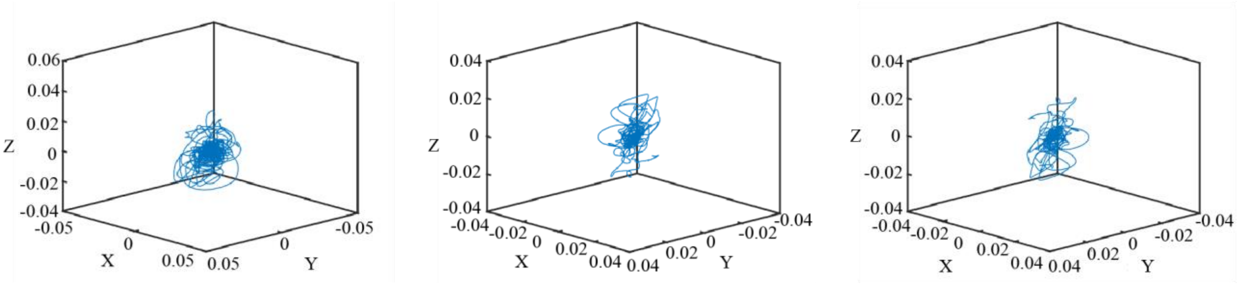

(d) Mooring 3 (e) Mooring 4 (f) Mooring 5

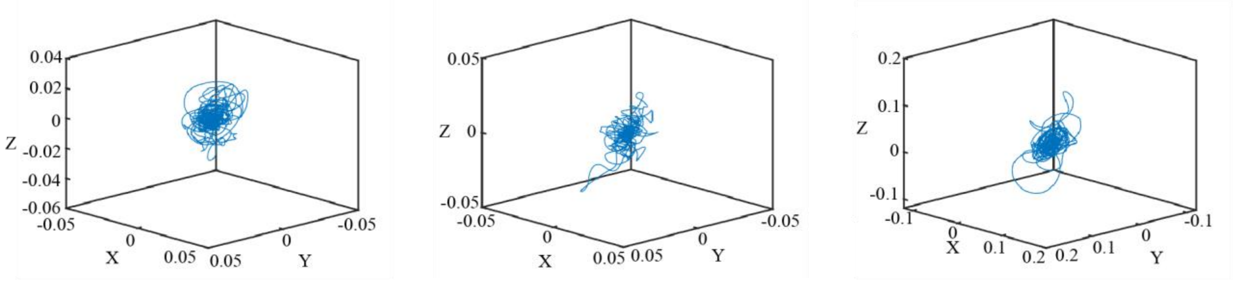

(g) Mooring 6 (h) Mooring 7 (i) Mooring 8

Figure.13 Phase diagram of dynamic response signal of each mooring

Analysis of Figure 13 shows that the phase diagrams of normal moorings and faulty moorings are significantly different, with different morphologies, but all of them are in the shape of hairy spheres, which show a non completely random and non completely periodic response, indicating that the dynamic response signals of each mooring have significant chaotic characteristics. In order to quantify the strength of the chaotic characteristics, the Lyapunov exponent of each mooring signal was calculated and the results are shown in Table 8.

Table 8

Lyapunov exponent of mooring signals

Mooring type	Value	Mooring type	Value
Normal state	0.00558	Mooring 5	0.01394
Mooring 1	0.00816	Mooring 6	0.01218
Mooring 2	0.00919	Mooring 7	0.01154
Mooring 3	0.01223	Mooring 8	0.00834
Mooring 4	0.01448	-	-

It can be seen from Table 8 that the Lyapunov exponent of the response signal of the bow of the platform is greater than 0 when each mooring is in creep, indicating that they have chaotic characteristics in different degrees. At the same time, it can be seen that because the dynamic response signal of the normal mooring is more stable and the nonlinearity is weaker, its Lyapunov exponents are all smaller than those of the faulty mooring.

4.2 Model Training

In order to extract the nonlinear feature signals in the chaotic sequences and accurately perform fault classification, the platform yaw response signals are divided into training set, validation set and test set in the ratio of 8:1:1, and they are input into the CNN model for training, and the number of iterations is set to 140, with 100 each. The creep mooring fault classification accuracy and loss curves are shown in Figure 14.

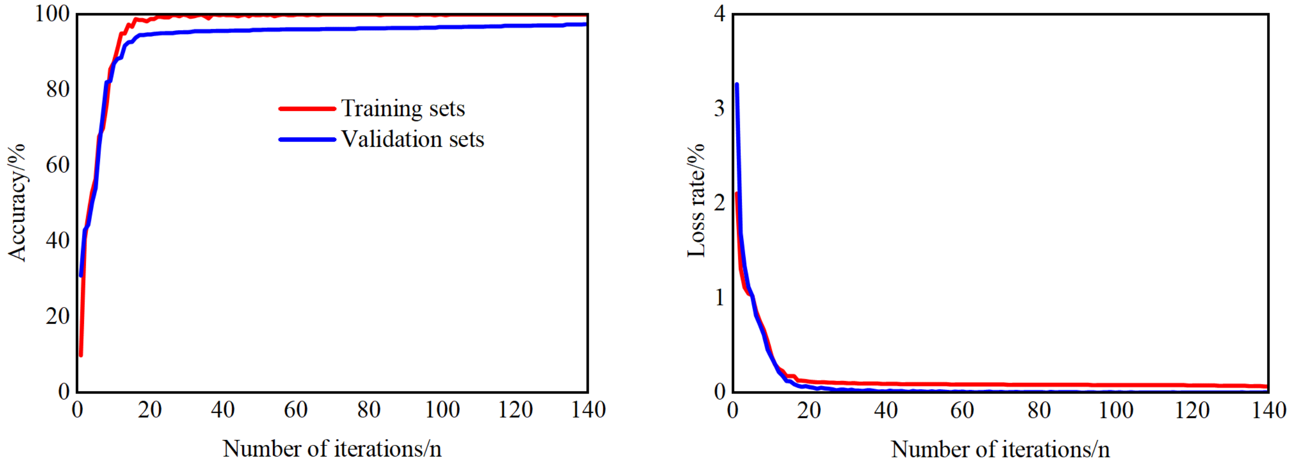

(a) Accuracy (b) Loss rate curve

Figure.14 Curve of training results

As shown in Figure 14, the state identification can be performed better by using convolutional neural network, and the classification accuracy and loss rate almost stop changing when the iteration reaches 22, at which time the accuracy is as high as 98.86% and the loss rate is 0.0517, and the results show that the method can extract a more pure dynamic response signal.

Meanwhile, in order to more clearly demonstrate the classification effect of the model on creep mooring location, the confusion matrix was introduced for analysis, and the results are shown in Figure 15. In the figure, the horizontal axis is the predicted category, the vertical axis is the actual category, and the main diagonal line indicates the number of correctly classified samples.

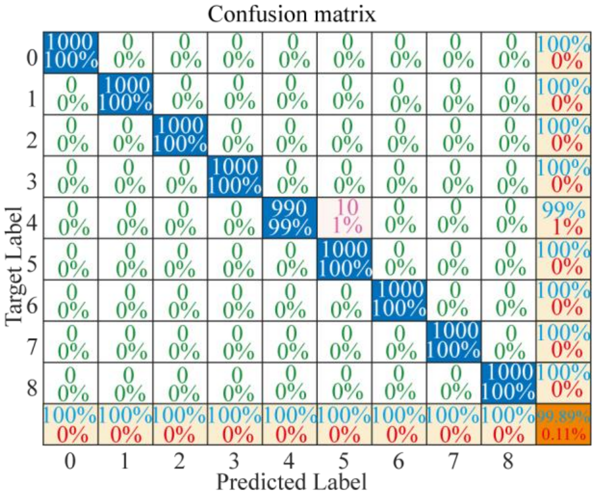

	0	1	2	3	4	5	6	7	8	
0	1000 100%	0 0%	0 0%	0 0%	0 0%	0 0%	0 0%	0 0%	0 0%	100% 0%
1	0 0%	1000 100%	0 0%	0 0%	0 0%	0 0%	0 0%	0 0%	0 0%	100% 0%
2	0 0%	0 0%	1000 100%	0 0%	0 0%	0 0%	0 0%	0 0%	0 0%	100% 0%
3	0 0%	0 0%	0 0%	1000 100%	0 0%	0 0%	0 0%	0 0%	0 0%	100% 0%
4	0 0%	0 0%	0 0%	0 0%	990 99%	10 1%	0 0%	0 0%	0 0%	99% 1%
5	0 0%	0 0%	0 0%	0 0%	0 0%	1000 100%	0 0%	0 0%	0 0%	100% 0%
6	0 0%	0 0%	0 0%	0 0%	0 0%	0 0%	1000 100%	0 0%	0 0%	100% 0%
7	0 0%	0 0%	0 0%	0 0%	0 0%	0 0%	0 0%	1000 100%	0 0%	100% 0%
8	0 0%	0 0%	0 0%	0 0%	0 0%	0 0%	0 0%	0 0%	1000 100%	100% 0%
	100% 0%	100% 0%	100% 0%	100% 0%	100% 0%	100% 0%	100% 0%	100% 0%	100% 0%	99.89% 0.11%

Figure.15 Multi-class confusion matrix of diagnosis results

As can be seen from Figure 15, only mooring 4 creep was misclassified as mooring 5 creep, and the rest of the creep mooring positions were classified without errors, the overall classification accuracy was high.

4.3 Model Visualization

To show the superior feature extraction and classification ability of the proposed method in this paper, t-SNE [35] was used to reduce the dimensionality and visualize the fault classification results. The results are shown in Figure 16.

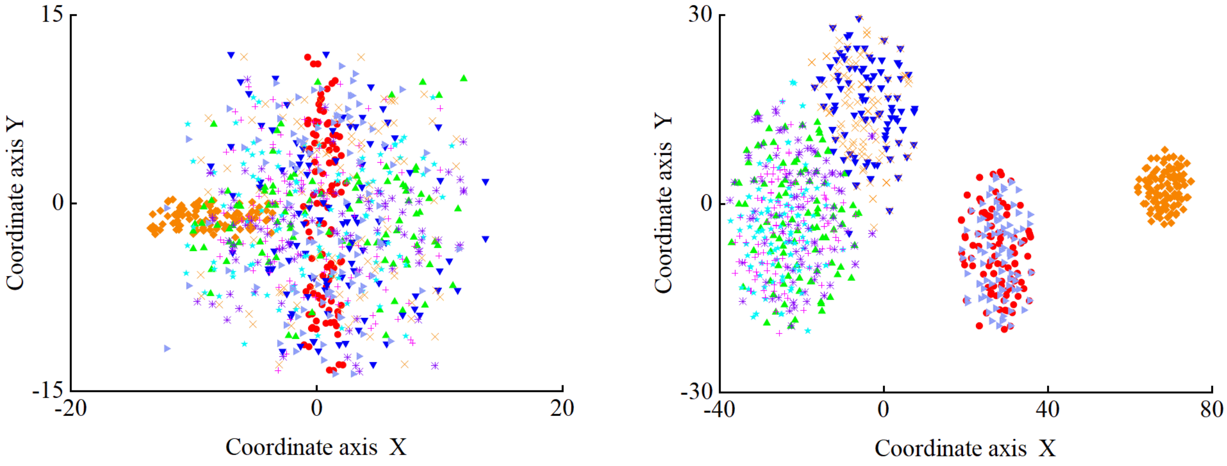

(a) Convolutional layer 1

(b) Convolutional layer 2

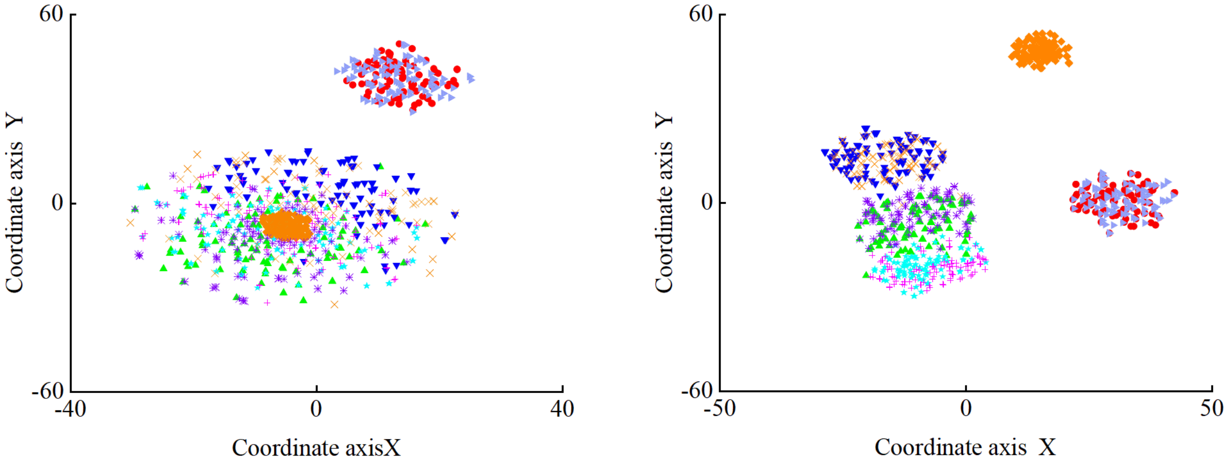

(c) Convolutional layer 3

(d) Convolutional layer 4

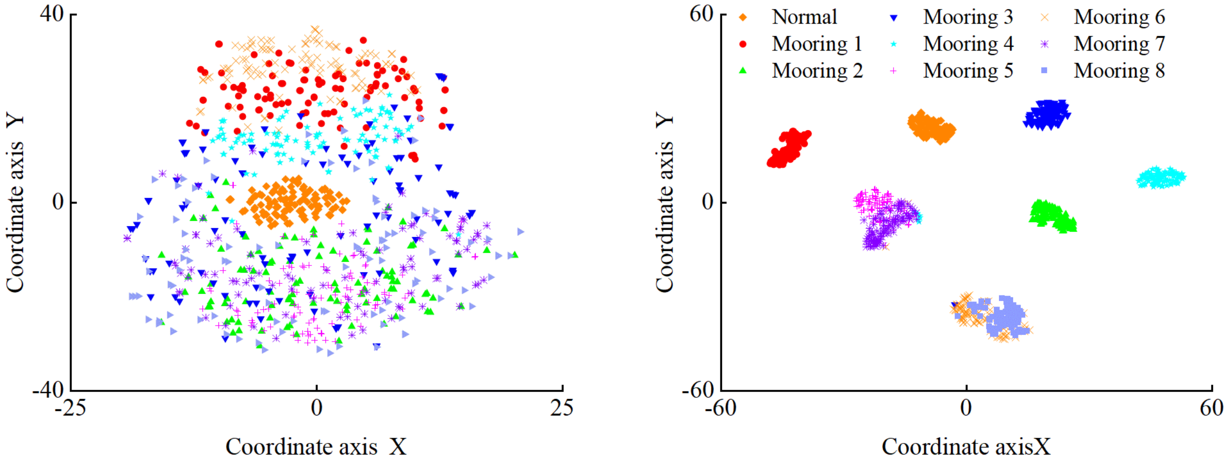

(e) Convolutional layer 5

(f) Fully connected layer

Figure.16 Visualization results of each convolutional layer

As can be seen from Figure 16, with the increase of convolutional layers, the neural network gradually captures the data features in depth, and the class spacing of different creep moorings gradually increases, and the phenomenon of point cluster separation has appeared in convolutional layer 2, in which normal moorings have been clearly separated; in the fully connected layer, different creep moorings have been able to be clearly distinguished, indicating that CNN can extract pure nonlinear information from chaotic sequences.

In addition to this, to further understand the properties of the learned features of the convolutional layers, the feature signals extracted by convolutional layer 1 and convolutional layer 5 are visualized and their chaotic properties are analyzed, and the attractor trajectories are shown in Figure 17.

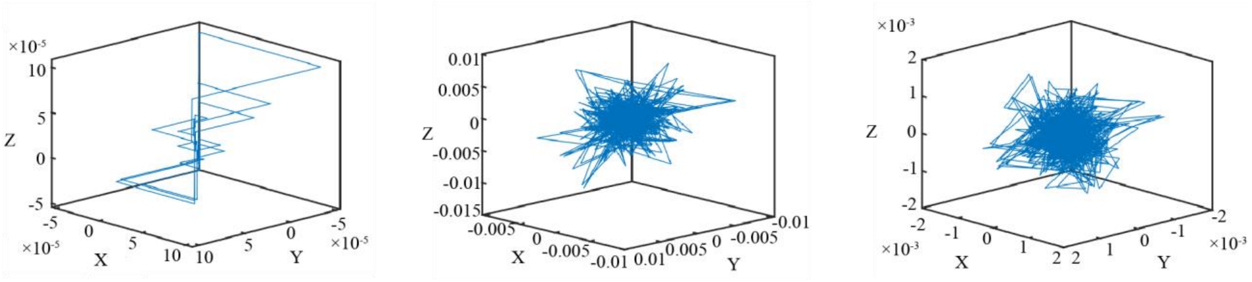

(a) Normal (b) Mooring 1 (c) Mooring 2

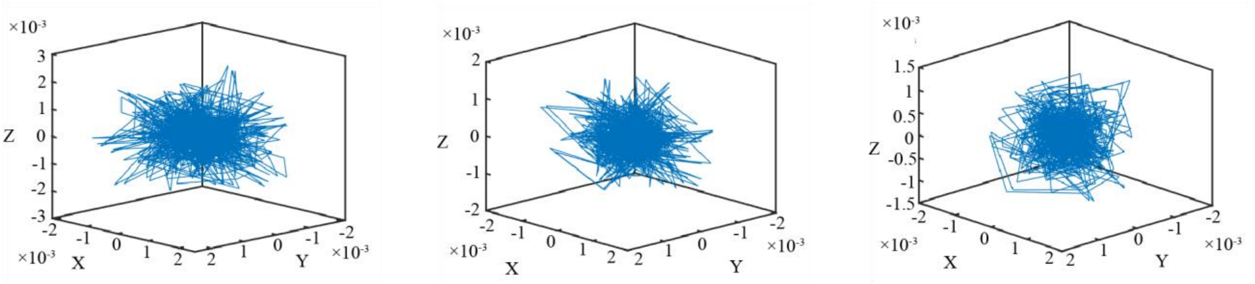

(d) Mooring 3 (e) Mooring 4 (f) Mooring 5

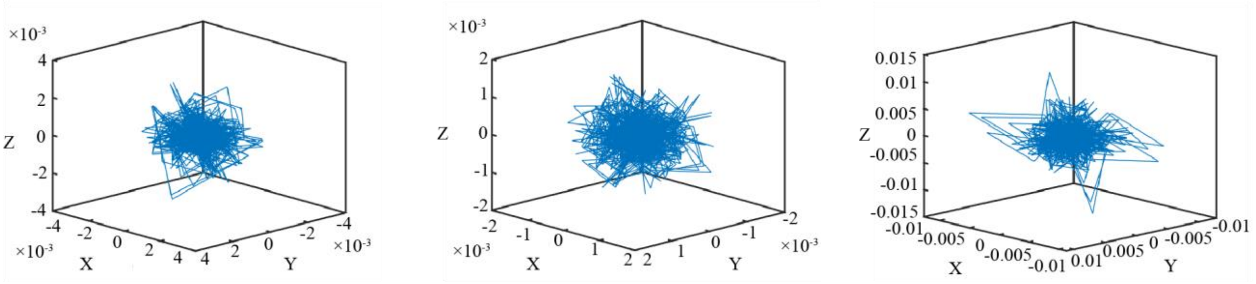

(g) Mooring 6 (h) Mooring 7 (i) Mooring 8

(I) Convolutional layer 1

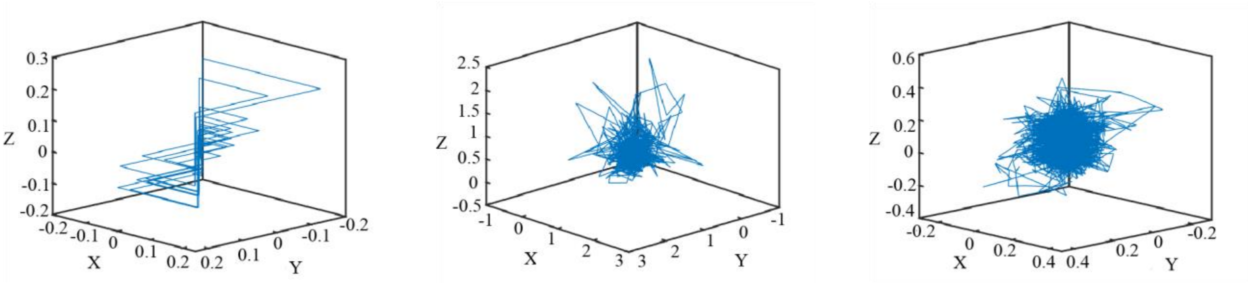

(j) Normal (k) Mooring 1 (l) Mooring 2

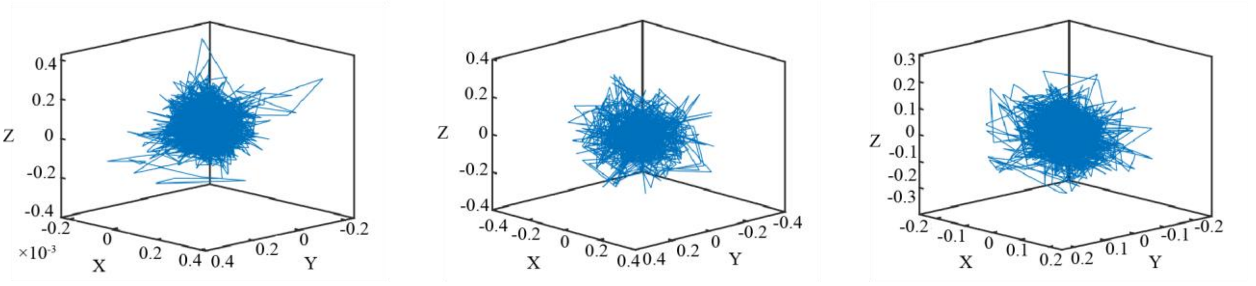

(m) Mooring 3 (n) Mooring 4 (o) Mooring 5

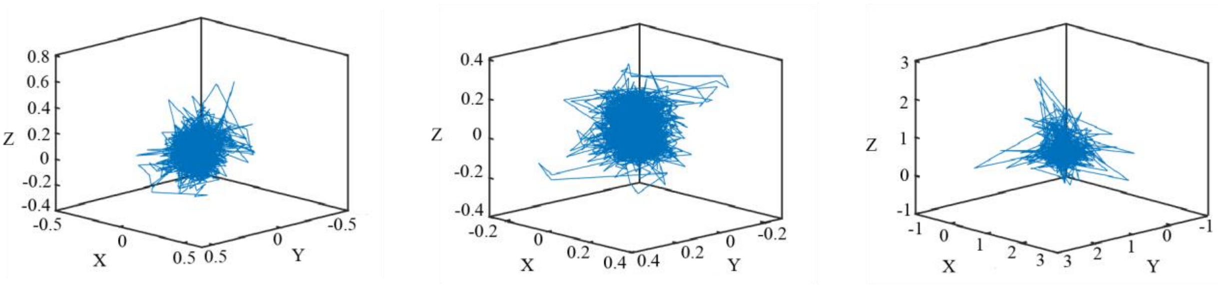

(p) Mooring 6 (q) Mooring 7 (r) Mooring 8

(II) Convolutional layer 5

Figure.17 Phase diagram of different convolution layers

From Figure 17, it can be seen that the attractor trajectories of different creep moorings have significant chaotic characteristics, and the attractors develop from chaotic disorder toward orderliness as the number of convolution layers increases. To quantify the weakening of the chaotic characteristic and the enhancement of the purity of the dynamic response of the platform, the Lyapunov exponents of the original data of each creep mooring and the convolution layer 5 are calculated, and the results are shown in Figure 18.

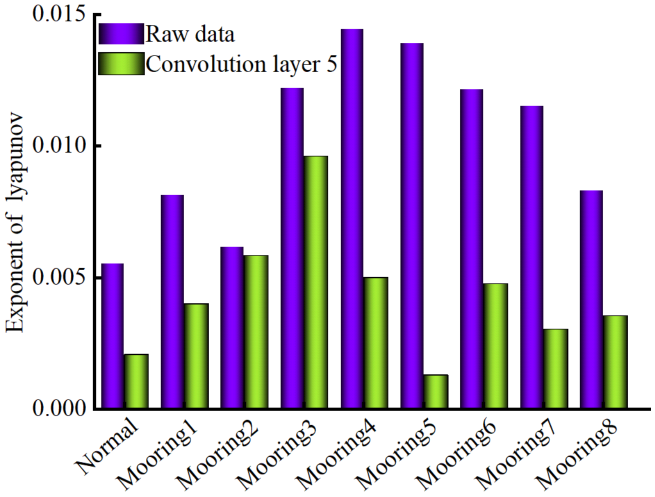

Figure.18 The original data and the Lyapunov exponent of convolution layer 5

When $\lambda > 0$, the system has chaotic characteristics and its nonlinearity increases with increasing λ [28]. From Figure 18, it can be seen that the Lyapunov exponent calculated from the original data of the moorings in different states after phase space reconstruction is larger than the Lyapunov exponent calculated from the data extracted in convolution layer 5 , and it can be shown that the nonlinearity of the dynamic response of the platform yaw is reduced after the CNN model convolutional pooling and other operations, indicating that the proposed method in this paper can extract purer nonlinear information.

4.4 Performance under different noise

In this section, we will examine and discuss the accuracy of the developed diagnostic system. The test data used above are under noise-free conditions. The awgn function in MATLAB [36] is used to add different sizes of noise to the original experimental data to test the performance of the neural network model applied in this paper under real conditions.

As shown in Figure 19, there is a significant difference between the original signal (blue line), the signal with 0 dB Gaussian noise (red line), and the signal with -4 dB Gaussian noise (black line). Noise is a common problem during the actual operation of wind turbines. It is what alters the distribution of the data, thus masking the fault characteristics of the wind turbine and affecting the diagnostic accuracy of the model. The performance of the dynamic response signals analyzed using the method proposed in this paper at noise levels of -4 dB to 12 dB is shown in Figure 19.

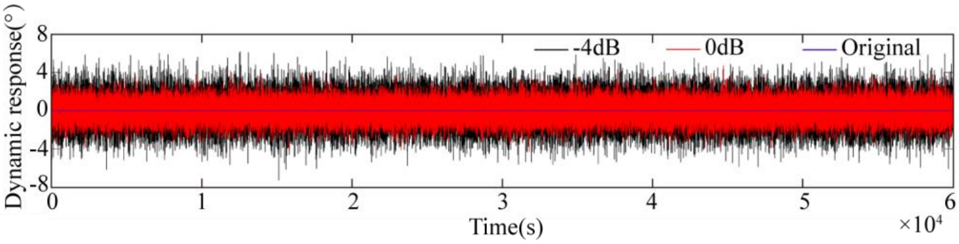

Figure.19. Time domain diagram of fault signal under different noise

As can be seen from Figure 19, when the noise gradually increases, the dynamic response signal of the wind turbine platform is gradually masked by the noise, changing the characteristics of the original data, which can affect the diagnostic accuracy of the model.

To study the effect of different sizes of noise, the performance of the diagnostic model for fault identification when the noise level is -4 dB to 12 dB is analyzed using the method proposed in this paper, and the results are shown in Figure 20.

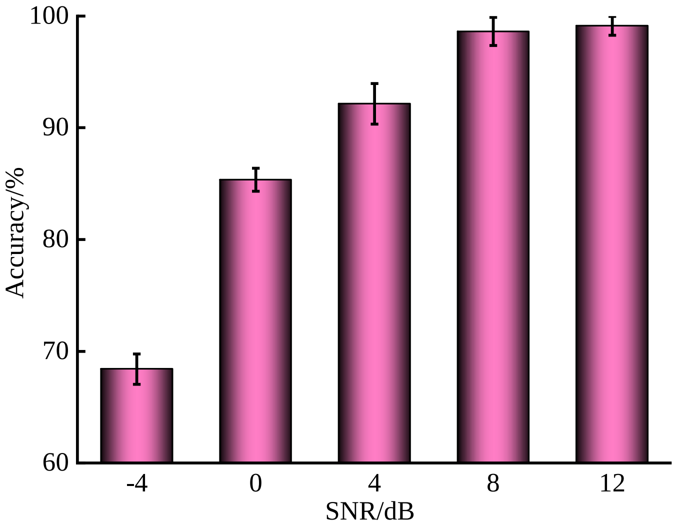

Figure.20 The accuracy of CNN-t-SNE under different noisy environments

As can be seen from Figure 20, when the noise gradually increases, the dynamic response signal of the floating wind turbine platform is gradually masked by the noise, changing the characteristics of the original data, which can affect the diagnostic accuracy of the model.

To study the effect of different sizes of noise, the performance of the diagnostic model for fault identification when the noise level is -4 dB to 12 dB is analyzed using the method proposed in this paper, and the results are shown in Figure 16.

4.5 Performance of different methods

In addition, in highlighting the superiority of the proposed method in this paper, Table 9 compares the fault diagnosis of BN, SVM, ICA-SVM, PCA-SVM, CNN and CNN-t-SNE [29] for signals with different SNRs. In order to show the effect of fault diagnosis more clearly, the classification accuracy line graph is shown in Figure 21.

Table 9

Methods compared results under different noisy environment

SNR/dB	Methods/%					
	BN	SVM	ICA-SVM	PCA-SVM	CNN	CNN-t-SNE
-4	47.31	55.79	63.67	59.48	63.98	69.85
0	70.16	76.89	79.17	82.39	80.21	85.63
4	90.51	90.23	91.87	91.68	93.14	92.67
8	92.96	91.85	94.23	94.21	99.23	99.56
12	90.59	91.75	98.19	98.99	99.99	99.99

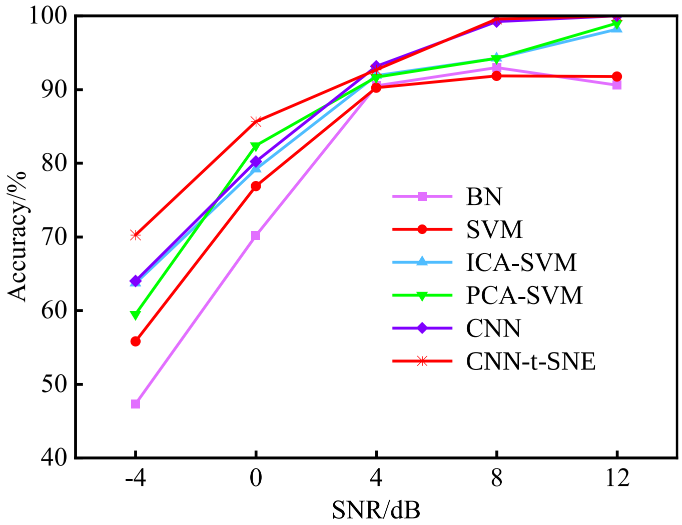

Figure. 21 Methods compared results under different noisy environment of the line chart.

As shown in Figure 21, the proposed method in this paper has the best performance in a noisy background compared to the other five methods. The shortcoming of the other methods is that although they perform well at low noise levels, the accuracy is extremely low in a strong noise environment. Under different noise scenarios, CNN-t-SNE has the highest accuracy (70.25%) for classification in a large noise (-4dB) environment, which is higher than BN (47.31), SVM (55.79%), ICA-SVM (63.67), PCA-SVM (59.48), and CNN (63.98). It is worth noting that CNN-based methods have higher accuracy compared with SVM methods because CNNs have stronger generalization ability than SVMs. SVM methods are shallow learning, and shallow learning methods in general have insufficient generalization ability and are relatively poor.

5 Conclusion

For extreme environment in which floating wind turbines are being used, the mooring is easy to creep, which will accelerate corrosion and lead to mooring failure. This paper analyzes the dynamic response of platform bow rocking based on deep learning and chaos theory, focusing on whether creep occurs in the mooring and identifying the location where creep occurs in the mooring, which is important to prevent mooring failure in advance and ensure the safe and stable operation of wind turbine. Based on the Barge platform 5 MW floating wind turbine, the following conclusions can be drawn.

(1) During the stage of mooring creep, the platform response changes very little, but the response increases sharply after mooring failure, where the bow rocking response is more sensitive.

(2) The convolution neural network is used to extract the characteristics of the dynamic response signal of the offshore wind turbine platform, and the Lyapunov exponent of the signals extracted from each convolutional layer is analyzed, and the results show that the dynamic response signal of the offshore wind turbine platform decays nonlinearly.

(3) After dimensionality reduction using t-SNE, the creep mooring positions can be clearly distinguished by the platform yaw response signal.

(4) Combining attractor trajectories with Lyapunov exponents can reflect the chaotic characteristics of dynamic signals and can quantitatively represent that CNN can extract pure nonlinear information from chaotic sequences.

6 Future work

In this study, the dynamic response of the FWT platform was investigated. The proposed intelligent damage detection model named CNN-t-SNE automatically extracts the advanced features from the Chaotic Space and finally locates which mooring has occurred creep, which is important to prevent mooring failure and ensure the normal operation of the FWT. The following may be undertaken in the future:

(1) Because of the strong nonlinearity of the dynamic response signal of the FWT platform, a multi-scale convolutional neural network is subsequently considered and a feature attention mechanism is added to analyze the signal.

(2) This paper is a study of the mooring system of 5MW FWT platform, and the subsequent consideration of comparing the same and different vibration signals of 10MW and 5MW FWT platforms.

(3) In this paper, we assume that the ocean current is uniform flow, and then we will study how the dynamic response signal of the FWT platform changes when the ocean current is nonuniform.

(4) This paper is to study the effect of mooring on the FWT platform, and subsequently will also study the joint effect of tendon and mooring on the FWT platform.

Acknowledgements

The authors would like to acknowledge the support of National Natural Science Foundation of China (Grand No. 52006148, 51976131 and 52106262).

References:

[1] LIU W Y, ZHANG W H, HAN J G, et al. A new wind turbine fault diagnosis method based on the local mean decomposition[J]. Renewable Energy, 2012, 48: 411-415.

[2] LUIZ D A T L, MILAD S, LUIZ P D F A, et al. Influence of the WRF model and atmospheric reanalysis on the offshore wind resource potential and cost estimation: A case study for Rio de Janeiro State [J]. Energy, 2022.

[3] ABDELBAKY M A, LIU X, JIANG D. Design and implementation of partial offline fuzzy model-predictive pitch controller for large-scale wind-turbines[J]. Renewable Energy, 2020, 145: 981-996.

[4] KONG X, MA L, WANG C, et al. Large-scale wind farm control using distributed economic model predictive scheme[J]. Renewable Energy, 2022, 181: 581-591.

[5] PHAM T D, DINH M C, KIM H M, et al. Simplified Floating Wind Turbine for Real-Time Simulation of Large-Scale Floating Offshore Wind Farms[J]. Energies, 2021, 14(15).

[6] HUANG L, SHEN D, FU Y, et al. Research on the Wake Effect of Floating Wind Turbine[C]// 2020 5th Asia Conference on Power and Electrical Engineering (ACPEE). 2020.

[7] DUPUIS R. Application of Oil Debris Monitoring for Wind Turbine Gearbox Prognostics and Health Management[C]// Annual Conference of the PHM Society. 2010.

[8] DYBALA J, ZIMROZ R. Rolling bearing diagnosing method based on Empirical Mode Decomposition of machine vibration signal[J]. Applied Acoustics, 2014, 77: 195-203.

[9] MOGHADAM F K, NEJAD A R. Theoretical and experimental study of wind turbine drivetrain fault diagnosis by using torsional vibrations and modal estimation-ScienceDirect[J]. Journal of Sound and Vibration, 2021.

[10] RINALDI G, THIES P R, JOHANNING L. Current Status and Future Trends in the Operation and Maintenance of Offshore Wind Turbines: A Review[J]. Energies, 2021, 14(9).

[11] TIMERMAN G J, CAMPOS M A D, NISHIMOTO K, et al. Coupled dynamic and static analysis of typhoon TLP accident during extreme environmental conditions [C]// International Conference on Offshore Mechanics and Arctic Engineering. Estoril: OMAE, 2008.

[12] LI Y, ZHU Q, LIU L, et al. Transient response of a SPAR-type floating offshore wind turbine with fractured mooring lines [J]. Renewable Energy, 2018, 122: 576–588.

[13] BAE Y H, KIM M H, KIM H C. Performance changes of a floating offshore wind turbine with broken mooring line [J]. Renewable Energy, 2017, 101: 364–375.

[14] YANG M D, TENG B, XIAO L F. Full time domain nonlinear coupled dynamic analysis of a truss spar and its mooring/riser system in irregular wave[J]. Science China Physics Mechanics & Astronomy, 2014, 57(1): 152-

165.

[15] KREUTZ M, ALLA A A, EISENSTADT A, et al. Ice detection on rotor blades of wind turbines using RGB images and convolutional neural networks[J]. Procedia CIRP, 2020, 93: 1292-1297.

[16] CAO Z, XU J, XIAO W, et al. A novel method for detection of wind turbine blade imbalance based on multi-variable spectrum imaging and convolutional neural network[C]// 2019 Chinese Control Conference. IEEE, 2019.

[17] GUO Y F, QUAN W M, WANG W Y, et al. Crack diagnosis method of wind turbine blade based on convolution neural network with 3D vibration information fusion[J]. Acta Optica Sinica, 2020, 40(22): 140-148.

[18] HEMMATI A, OTERKUS E, BARLTROP N, et al. Fragility reduction of offshore wind turbines using tuned liquid column dampers[J]. Soil Dynamics and Earthquake Engineering, 2019, 125: 105705.

[19] JONKMAN J, MATHA D. Quantitative comparison of the responses of three floating platforms[J]. Australian Historical Studies, 2010, 32(3): 351-355.

[20] JONKMAN J, MATHA. Dynamics of offshore floating wind turbines-analysis of three concepts[J]. Wind Energy, 2011, 14(4): 557-569.

[21] YE K, JI J C. Current, wave, wind and interaction induced dynamic response of a 5 MW Spar-type offshore direct-drive wind turbine[J]. Engineering Structures, 2019, 178: 395-409.

[22] MORIARTY P J, HANSEN A C. AeroDyn Theory Manual[R]. Colorado: National Renewable Energy Laboratory, 2010.

[23] LACKNER M A, ROTEA M A. Structural control of floating wind turbines[J]. Mechatronics, 2011, 21(4): 704-719.

[24] JONKMAN J M. Dynamics Modeling and Loads Analysis of an Offshore Floating Wind Turbine[J]. Dissertations & Theses Gradworks, 2007.

[25] JONKMAN B J, BUHL M L. TurbSim User’s Guide[R]. Colorado: National Renewable Energy Laboratory, 2005.

[26] Xu Z F, Li C, Yang Y. Fault diagnosis of rolling bearings using an Improved Multi-Scale Convolutional Neural Network with Feature Attention mechanism[J]. ISA Transactions, 2021, 110: 379-393.

[27] GOODFELLOW I, BENGIO Y, COURVILLE A. Deep Learning[M]. Cambridge, MA: The MIT Press, 2016.

[28] STERMAN J D. Deterministic chaos in models of human behavior: Methodological issues and experimental results[J]. System Dynamics Review, 1988, 4(1): 148-178.

[29] LU S D, SIAN H W, WANG M H, et al. Fault diagnosis of power capacitors using a convolutional neural network combined with the chaotic synchronisation method and the empirical mode decomposition method[J]. IET SCIENCE MEASUREMENT & TECHNOLOGY, 2021, 15(7): 551-561.

[30] ABARBANEL H D I, BROWN R, SIDOROWICH J J, et al. The analysis of observed chaotic data in physical systems[J]. Reviews of modern physics, 1993, 65(4): 1331-1392.

[31] GE H, ZHANG S. Liouville-type theorems on the complete gradient shrinking Ricci solitons[J]. North-Holland,

2018, 56: 42-53.

[32] WOLF A, SWIFT J B, SWINNEY H L, et al. Determining Lyapunov exponents from time series[J]. Physica D, 1985, 16(2): 285-371.

[33] SAKARIS C S, M, Yang BASHIR Y, et al. Diagnosis of damaged tendons on a 10 MW multibody floating offshore wind turbine platform via a response-only functional model based method[J]. Engineering Structures, 2021, 242(3): 112384.

[34] JIAO J L, HUANG S X, TEZDOGAN T, et al. Slamming and green water loads on a ship sailing in regular waves predicted by a coupled CFD–FEA approach[J]. OCEAN ENGINEERING, 2021, 241.

[35] LAURENS V D M. Accelerating t-SNE using tree-based algorithms[J]. Journal of Machine Learning Research, 2014, 15(1): 3221-3245.

[36] MC H K. Modelling and Analysis of 8psk modulation scheme using awgn channel for wcdma system[J]. International Journal of Advanced Research in Computer Science & Electronics Engineering, 2013, 2(2): 403-406.